Diploma Thesis R 1314 D

Optimization of the InSight HP³-Mole

Torben Wippermann

September 2013

pages: 055
pictures: 042
tables: 002

Prof. Dr.-Ing. Peter Vörsmann
Technical University of Braunschweig
Institute of Aerospce Systems
Hermann-Blenk-Straße 23, 38108 Braunschweig

German Aerospace Center (DLR)
Institute of Space Systems
Department of Explorations Systems
Robert-Hooke-Straße 7, 28359 Bremen

Optimization of the InSight HP³-Mole

Diploma Thesis

Torben Wippermann (matriculation number 2891468)

Institute of Aerospace Systems
Technical University of Braunschweig

September 2013

Reviewer: Prof. Dr.-Ing. Peter Vörsmann
Institute of Aerospace Systems
Technical University of Braunschweig

Dr.-Ing. Carsten Wiedemann
Institute of Aerospace Systems
Technical University of Braunschweig

Supervisor: Dr. Tim van Zoest
Department of Explorations Systems
Institute of Space Systems
German Aerospace Center (DLR) Bremen

Dipl.-Ing. (FH) Olaf Krömer
Department of Explorations Systems
Institute of Space Systems
German Aerospace Center (DLR) Bremen

(Aufgabenstellung Seite 1)

(Aufgabenstellung Seite 2)

Affidavit

I affirm in lieu of oath, that I have made the following thesis independently and only with the aid of the specified literature.

Bremen, 17th of September 2013

Overview

The German Aerospace Center (DLR) is providing the HP³-payload for the InSight-Mission of NASA. InSight is the 12th part of the Discovery program and is supposed to investigate the seismic activities, geodesy and heat transport of the interior of the mars [RD 13]. HP³ is the abbreviation for Heat Flow & Physical Properties Package. It consists of a heat probe that will measure the heat flow of the mars in depths of up to five meters. To get the probe there it is integrated in the HP³-Mole. The HP³-Mole is a non-rotating drill that acts like a self-hammering nail. An internal hammering mechanism, which is a three mass system, is pushing the Mole with every stroke deeper in the Martian soil. These three masses are linked to each other via two springs. In this thesis, several methods of improving the advancing speed of the Mole are investigated. The changes that provide a high enhancement will be integrated in the Prototype-Model, resp. the Engineering-Model of the Mole.

At first the optimal mass ratio of the three masses will be examined, which is composed of the equations of the movement and strokes. For this mass ratio the mass of the outer hull will be adjusted. First assessments show that the mass of the outer hull of the existing Mole is too high. Besides the reducing of the mass, the outer hull should be built as thin as possible to minimize the cross section of the mole. This will decrease the penetrating resistance of the soil. In the new outer hull a way to integrate all the payloads and electronics should be realized too. Another possibility to enhance the advancing speed is to change the springs in the hammering mechanism. Further changes of the three masses and the two springs will be considered in relation to the possible improvement of the hammering process. The changes will be entered in an existing simulation to calculate the resulting improvement in the penetration progress.

In the next step the cylindrical cam, which is used to tense the main spring, will be redesigned. The aim of the change is to increase the height of the cylindrical cam. This has a direct effect on the energy of the outer hull when hitting on the soil. The new designed cylindrical cam has a complex shape that needs to be inserted in the simulation. The penetrating progress will be simulated too.

Besides of the thinner Mole the shape of the tip of the Mole has a great influence on the soils penetrating resistance. In the previous designs the tip has the shape of a cone. This will be compared with other tips like flats, spheres, ogives and other cone angles.

In addition all the changes will be integrated in the 3D-CAD-model. The assembling of the Mole should be considered during the designing process and should be as easy as possible.

Contents

List of abbreviations

BB	Breadboard
CNES	Centre National d'Études Spatiales
DLR	Deutsches Zentrum für Luft- und Raumfahrt (German Aerospace Center)
ESA	European Space Agency
ETH	Eidgenössische Technische Hochschule (Swiss Federal Institute of Technology)
HP³	Heat Flow & Physical Properties Package
InSight	Interior Exploration using Seismic Investigations, Geodesy and Heat Transport
IPGP	Institut de Physique du Globe de Paris
JPL	Jet Propulsion Laboratory
MMS-Mole	Micro Mass Spectrometer Mole
MMUM	Moon/Mars Underground Mole
MPS	Max Planck Institut für Sonnensystemforschung (Max Planck Institute for Solar System Research)
MUPUS	Multi-Purpose Sensors for Surface and Sub-Surface Science
NASA	National Aeronautics and Space Administration
PLUTO	PLanetary Underground Tool
PT	Prototype
RISE	Rotation and Interior Structure Experiment
SEIS	Seismic Experiment for Interior Structure
SRC PAS	Space Research Centre of the Polish Academy of Science
STATIL	STAtic TILt acceleration measurement
TEM-A	Thermal Excitation and Measurement - Active

TEM-P	Thermal Excitation and Measurement – Passive
TiME	Titan Mare Explorer
TLM	Tether Length Measurement
WTS	Wind and Thermal Shield

Formula symbols

Latin alphabet

A_{ep}	projected cross-section for equal pressure ogive
A_{gb}	contact area between Guide block and Hammer support structure
A_{stroke}	contact area between Hammer and Tip
b_{gb}	width of Guide block at contact are
c_b	spring rate of Brake spring
c_f	spring rate of Force spring
c_{oc}	spring rate of Outer casing
c_s	spring rate of stand spring
C_h	HAACK ogive constant
d_{ha}	diameter of Hammer
$d_{i,t}$	inner diameter of Tip
$d_{i,oc}$	inner diameter of Outer casing
D	outer diameter of the Mole
$E_{1,kin}$	kinetic energy of hammer mass prior to primary stroke
$E_{1,kin,p}$	kinetic energy of hammer mass after primary stroke
$E_{12,kin}$	kinetic energy of hammer and actuator mass prior to secondary stroke
$E_{12,kin,p}$	kinetic energy of hammer and actuator mass after secondary stroke
$E_{2,kin}$	kinetic energy of actuator mass
$E_{3,kin}$	kinetic energy of housing mass for one hammering cycle
$E_{3,kin,1}$	kinetic energy of housing mass after primary stroke
$E_{3,kin,2}$	kinetic energy of housing mass after secondary stroke
$E_{diss,1}$	dissipative loss for primary stroke
$E_{diss,2}$	dissipative loss for secondary stroke
E_f	Force spring energy
E_s	stand spring energy
$E_{s,1}$	stand spring energy due to first stroke
$E_{s,2}$	stand spring energy due to second stroke
$E_{s,fric}$	energy losses due to friction
E_{Ti}	YOUNG's modulus of TiAl6V4
E_{X12}	YOUNG's modulus of MarvalX12
F_a	driving force
$F_{a,n}$	normal part of driving force
$F_{a,p}$	parallel part of driving force
F_{br}	load force of Roller
$F_{br,max}$	maximum load force of Roller

F_{eb}	reaction force on the Extension drive shaft bush
F_f	Force spring force
$F_{f,n}$	normal part of Force spring force
$F_{f,p}$	parallel part of Force spring force
F_{gb}	force on contact surface of Guide block due to torque
F_n	normal force between Roller and Cylindrical cam
$F_{r,12}$	friction force between hammer and actuator mass
$F_{r,23}$	friction force between actuator and housing mass
F_{stroke}	stroke force of first stroke
F_{wr}	side force of Roller
g	constant of gravitation
h_h	height of HAACK ogive
h_p	height of equal pressure ogive
h_s	height of secant ogive
k_f	force constant of Force spring
k_s	coefficient of restitution
$l_{b,c}$	compressed length of Brake spring
$l_{b,p}$	precompressed length of Brake spring
$l_{b,u}$	uncompressed length of Brake spring
$l_{b,u}^*$	virtual uncompressed length of Brake spring
l_{eb}	length of Extension drive shaft bush
$l_{f,c}$	compressed length of Force spring
$l_{f,p}$	precompressed length of Force spring
$l_{f,u}$	uncompressed length of Force spring
$l_{gb,1}$	length 1 of Guide block for contact area
$l_{gb,2}$	length 2 of Guide block for contact area
l_{oc}	length of Outer casing
l_r	contact length of Roller and Cylindrical cam
$l_{s,c}$	compressed length of stand spring
$l_{s,c,1}$	compressed length of stand spring due to first stroke
$l_{s,c,2}$	compressed length of stand spring due to second stroke
$l_{s,p}$	precompressed length of stand spring
$l_{s,p,1}$	precompressed length of stand spring prior to first stroke
$l_{s,p,2}$	precompressed length of stand spring prior to second stroke
$l_{s,u}$	uncompressed length of stand spring
L	length of Nose tip
m_1	hammer mass
m_2	actuator mass
m_3	housing mass
M_a	driving torque
$M_{a,max}$	maximum driving torque

$M_{b,ds}$	bending moment on Drive shaft
$P_{al,CA104}$	maximum allowed contact pressure for CA104
P_{eb}	specific bush load on Extension drive shaft bush
p_{gb}	contact pressure between Guide block and Hammer support structure
$p_{r,max}$	maximum HERTZian stress of Roller
r_a	outer radius of Cylindrical cam
r_{ar}	outer radius of Roller
$r_{gb,1}$	radius 1 of Guide block for contact area
$r_{gb,2}$	radius 2 of Guide block for contact area
$r_{gb,3}$	radius 3 of Guide block for contact area
$r_{gb,m}$	mid radius for contact area of Guide block
r_h	radius of HAACK ogive
r_i	inner radius of Cylindrical cam
r_m	mid radius of Cylindrical cam
r_p	radius of equal pressure ogive
r_s	radius of secant ogive
R	outer radius of the Mole
R_a	radius of the Roller at the outer radius of Cylindrical cam
R_i	radius of the Roller at the inner radius of Cylindrical cam
$R_{p0.2,X12}$	yield strength of MarvalX12
s	height of Cylindrical cam, Force spring displacement
s_1	height of Cylindrical cam at end of 1st segment
s_2	height of Cylindrical cam at end of 2nd segment / maximum height
s_s	stand spring displacement
s’	slope of Cylindrical cam
S_{eb}	safety factor for Extension drive shaft bush
S_{gb}	safety factor for Guide block
S_m	safety factor for driving torque
S_r	safety factor for Roller
S_t	safety factor for Tip
$U_{pot,ho}$	potential energy of housing after first stroke
v_1	velocity of hammer mass
v_{12}	velocity of hammer and actuator mass
$x_{gb,1}$	projected length 1 of Guide block for contact area
$x_{gb,2}$	projected length 2 of Guide block for contact area
$x_{gb,3}$	projected length 3 of Guide block for contact area
x_{oc}	deformation of Outer casing
z/b	ratio of depth and contact pressure width of Roller

Greek alphabet

α	inclination of Roller path
β_s	angle of slope of Cylindrical cam
θ	HAACK ogive variable
λ	secant ogive constant
μ_{ro}	coefficient of friction for rolling
μ_{ru}	coefficient of friction for slipping
ν	POISSON's ratio
ρ_s	ogive radius of secant shape
ρ_t	ogive radius of tangent shape
σ_t	maximum compressive stress of Tip
$\sigma_{fa,Ti}$	allowed fatigue stress of TiAl6V4
σ_{vg}	equivalent stress of Roller
$\sigma_{vg,max}$	maximum equivalent stress of Roller
σ_x	stress in local x-direction of Roller
σ_y	stress in local y-direction of Roller
σ_z	stress in local z-direction of Roller
ϕ_s	rotational angle of Cylindrical cam
$\phi_{s,1}$	rotational angle of Cylindrical cam at end of 1st segment
$\phi_{s,2}$	rotational angle of Cylindrical cam at end of 2nd segment / at the end of cam
χ	inclination angle of Mole

List of figures

List of tables

1. Introduction

This diploma thesis deals with the HP³-system which is part of the InSight mission. The background of this mission and previous Moles will be discussed in this chapter.

1.1. InSight

InSight was part of the final three proposed missions for NASA's Discovery Program. Its mission contains of a lander, similar to the Phoenix lander, which will land on Mars and will deploy two of the scientific payloads to the surface. The payloads, SEIS, HP³ and RISE, will investigate the interior of Mars to help understand the building of Mars and other terrestrial planets [RD 15].

The other two missions of the final round were the Titan Mare Explorer (TiME) and Comet Hopper. TiME's purpose was to examine a lake on Titan and measure its carbon cycle while sailing on the lake. Comet Hopper was intended to land and hop on the comet Wirtanen to investigate the comet on different places and observe it during its approach to the sun. In August 2012 InSight was selected to be the next mission of the Discovery Program [RD 13].

Fig. 1.1: TiME [RD 13] and Comet Hopper [RD 14]

1.1.1. The Discovery Program

NASA's Discovery Program has the purpose to realize many small and focused missions to explore the solar system. The missions should have a short development time and limited resources. Since 1992 the program was able to bring 11 missions to launch and has with InSight the twelfth mission in development. A few examples for these missions are the Mars Pathfinder, which contained the first rover on mars, Sojourner, and Deep Impact, which was the first to probe the surface of a comet. Stardust, which sampled cometary and interstellar

dust to return it to earth, and Kepler, the space telescope, were also part of this program [RD 12] [RD 13]. An overview of all started Discovery missions is shown in Fig. 1.2.

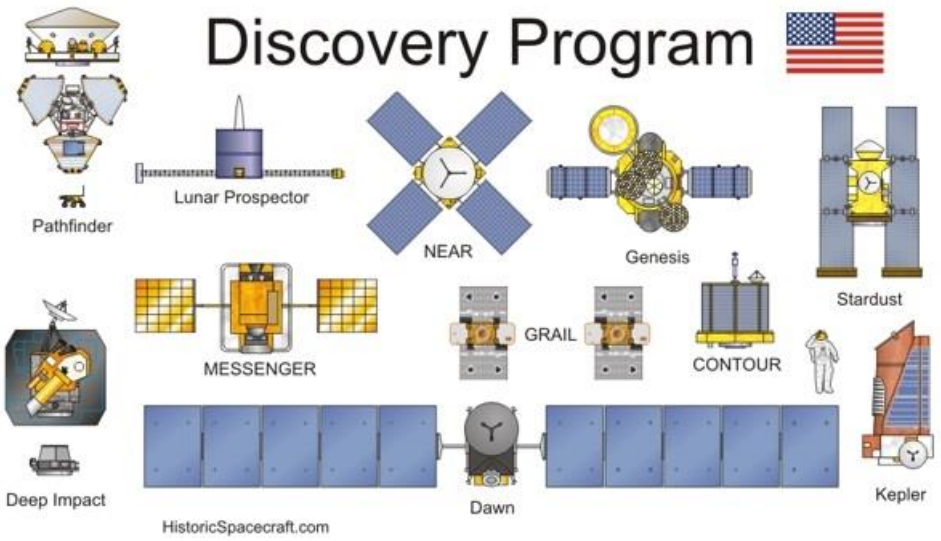

Fig. 1.2: Probes of the Discovery Program [RD 12]

Beneath the pure scientific use, the Discovery Program also distributes the educational and public outreach of the missions and their discoveries.

1.1.2. InSight mission, spacecraft and payloads

The InSight mission will launch in March 2016 and will land on Mars in September 2016. The lander is of the same type as the Mars lander for Phoenix, which successfully landed on Mars in 2007. The robotic arm that was used on the Phoenix lander to get a soil sample to the lander deck will also be used. Now it will be used to grab the SEIS and the HP³-instrument and place it next to the lander on the soil. Prior to that, cameras on the lander observe the deployment area to verify a suitable position for the instruments. SEIS, which will be the first instrument to deploy, is a seismometer build by the French space agency CNES with participation of the Institut de Physique du Globe de Paris (IPGP), the Swiss Federal Institute of Technology (ETH), the Max Planck Institute for Solar System Research (MPS), the Imperial College and the Jet Propulsion Laboratory (JPL). It will measure quakes and other internal processes of Mars. On top of SEIS the Wind and Thermal Shield (WTS) will be placed. It will separate SEIS from the Martian environment to reduce disturbances from the wind or temperature fluctuations. The next payload, to be deployed, is HP³, which will be described in detail in 1.1.3. It is developed by the German Aerospace Center (DLR). RISE, the last of the payloads, will stay on the lander. It measures the Doppler shift of Mars on the communication to Earth. This can be used to determine the precession and nutation of the Martian rotation. Several small instruments, like a radiometer or a magnetometer, will assist the measurements and help to specify the disturbances [RD 15].

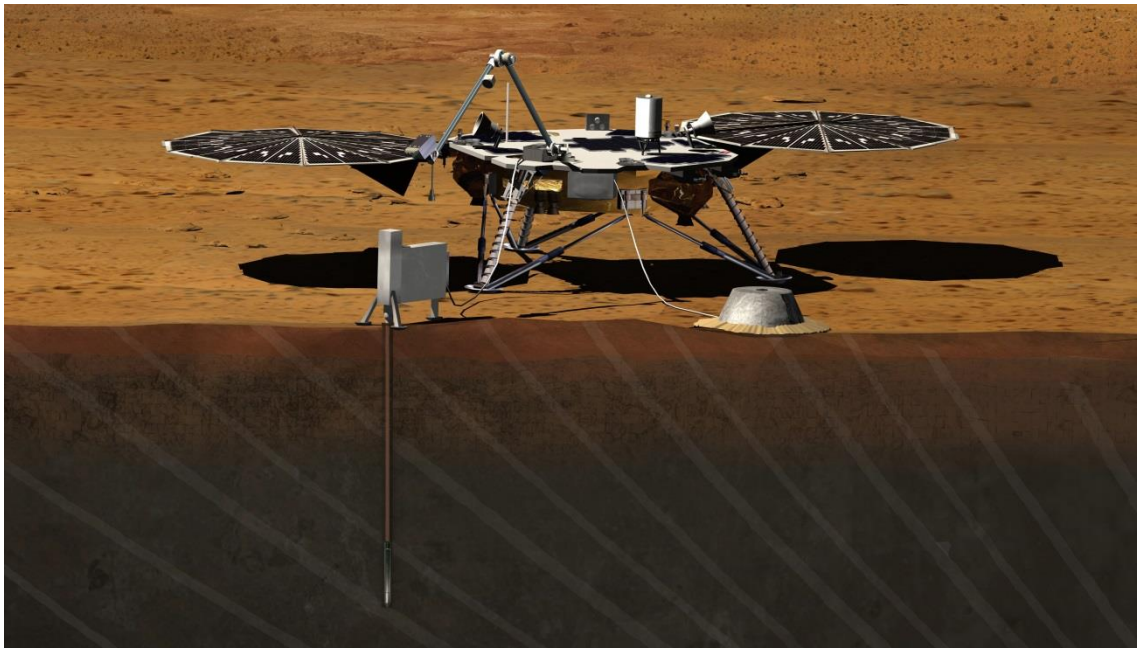

Fig. 1.3: InSight lander with HP³ (left front), SEIS (right front) and RISE (antennas on the lander) [RD 15]

The operational time of the instruments will be approximately two years. Fig. 1.3 shows the InSight mission after the deployment was executed.

1.1.3. Set up and scientific use of HP³

The HP³-system consists of the Mole (1), the Science tether (2), the Support structure (3), the Engineering tether (4), the Back End Electronics (BEE) box and a radiometer (not on the picture). The subsystems are displayed in Fig. 1.4 which shows a newer version of HP³ as Fig. 1.3.

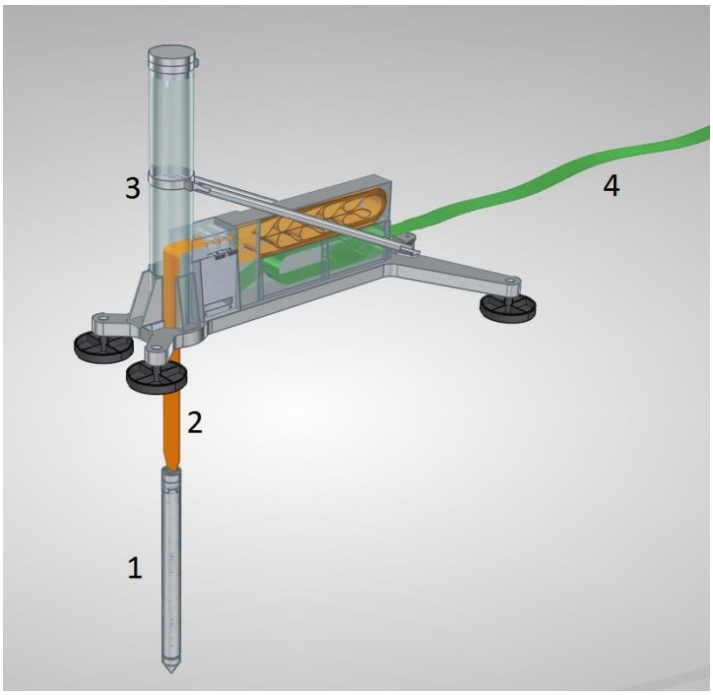

Fig. 1.4: Subsystems of HP³ [RD 3]

Mole

The Mole is a non-rotating drill that should penetrate itself into the Martian soil. For that purpose it uses an internal hammering mechanism. This hammering mechanism is the main topic of this diploma thesis and is described in detail in 1.2. The goal for the Mole is to reach at least 3 meter below surface. At maximum it can reach a depth of 5 meter. This depth is given as a limit to avoid that the Mole reaches possible ground water. The hammering mechanism will be operated in several intervals. After every 0.5 meter the hammering will be stopped, the Mole and the surrounding soil are resting for 48 hours and a measuring phase of 24 hours will take place. After that the Mole is penetrating again till it reaches the next measuring depth.

The Mole also includes a part of the TEM-sensors. TEM stands for Thermal Excitation and Measurement. Integrated in the outer hull are two heating foils, called TEM-A. They are the active part of the TEM-sensors. They will heat up the soil during the measuring phase. As the dissipating heat can be measured inside the foils, it is possible to read out the part of the thermal energy, which is transferred to the soil. With this measurement the conductivity of the Martian soil can be determined.

Another set of sensors is integrated on the inside of the Mole and behind the hammering mechanism. These sensors are called STATIL, STAtic TILt acceleration measurement. They consist of two accelerometers with two measuring axis each. Both accelerometers are positioned in a defined angle to each other and their positions are calibrated to the Mole. With this array the orientation of the Mole during the whole operation can be monitored. If the Mole is not penetrating straight downwards it can be observed with STATIL.

Science tether

The Science tether is constructed like a flexprint cable. It consists of three layers of Kapton tape with two layers of copper lines embedded. The copper lines are connected to the internal of the Mole so that it is possible to operate the Motor, STATIL and TEM-A. The read out of the data of TEM-A and STATIL will also be conveyed to the Support structure, where the Science tether is attached to. In addition to the operation of the Mole, the Science tether is functioned as a sensor itself. It builds the passive part of the TEM-sensors, TEM-P. TEM-P consists of several temperature sensors glued on one side of the Kapton. The second layer of copper lines is connected to each of the sensors separately. The purpose of the temperature sensors is to measure the temperature gradient inside the reached depth on Mars. As the sensors are fixed at defined positions and will record the temperature during each of the measuring phases, it is possible to derive the depth dependence of the geothermal heat. In combination with TEM-A it is possible to calculate the heat flow of Mars.

To reach the maximum depth, the Science tether has a length of 5 meter.

Engineering tether

The Engineering tether consists of three separate flexprint cables, which are fixed to each other in various points of their three meter length. The three tethers serve for the electrical connection of the Mole, the Science tether and the smaller subsystems inside the Support structure with the BEE box on the lander deck. It is stored in the Support structure and will be pulled out during the deployment with the robotic arm.

Support structure

The Support structure holds all the subsystems during launch, cruise, landing and deployment. The Mole is stored during these phases in the long tube on the left on Fig. 1.4. Apart from the Mole, Science tether and Engineering tether, the Support structure is equipped with launch locks for the Mole, heaters for the tethers and the Tether Length Measurement (TLM). TLM is reading a code of black squares on the Science tether, which can be translated in the length of the Science tether at the point it passes TLM. In addition with STATIL inside the Mole, it is possible to determine the position of the Mole during the whole penetrating process. This is mandatory to allocate the data of TEM to a verified depth [RD 16].

1.2. Principle of the HP³-Mole

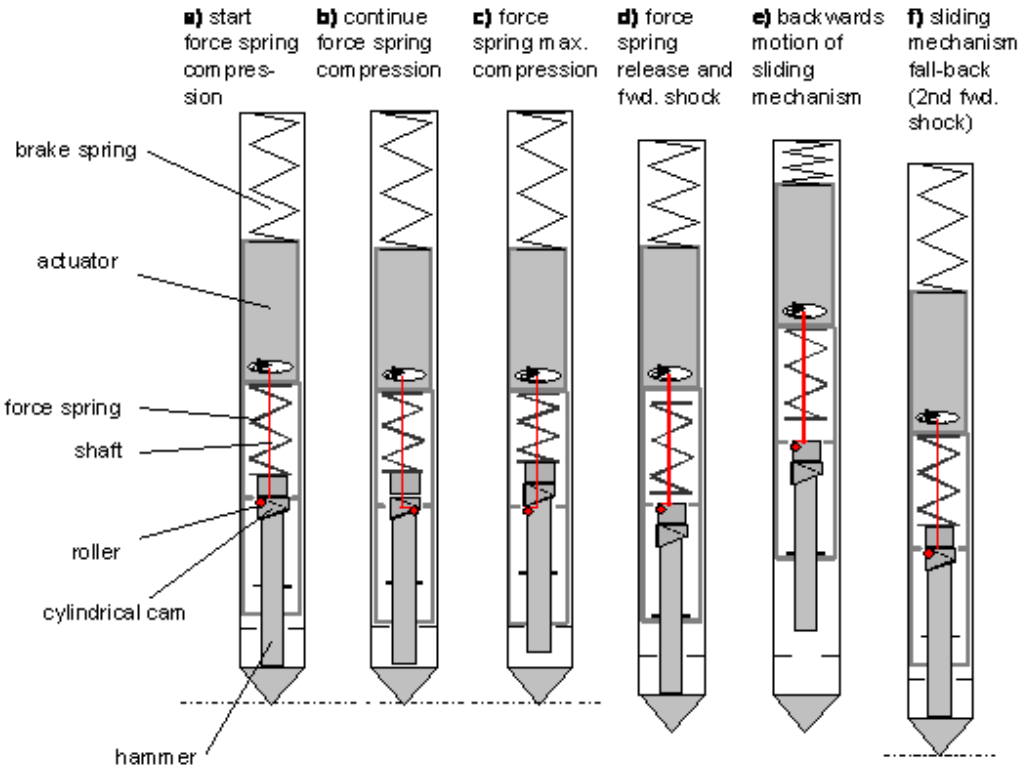

Fig. 1.5: Stages during operation of the HP³-Mole [RD 10]

This chapter will give an overview of the work principle of the hammering mechanism of the HP³-Mole. The mechanism consists of three masses and two springs between those masses. The masses are the hammer mass, the actuator mass and the housing mass. The two springs are the Force spring and the Brake spring. Fig. 1.5 shows the schematic setup of the hammering mechanism and the different stages during the operation.

At the beginning of a cycle (stage a) the Force spring and the Brake spring are precompressed and the three masses are not moving. The motor inside the actuator mass is attached to a drive shaft with a roller mounted perpendicular to the shaft. This roller is positioned on a cylindrical cam, which is part of the hammer mass. As the motor rotates the drive shaft, the roller is rolling on the ramp of the cylindrical cam. This pulls the hammer mass towards the actuator mass. With the Force spring between those two masses the spring is loading during the rotation of the drive shaft. This displacement continues during stage b and ends in stage c when the Roller is at the highest point of the cylindrical cam and the Force spring fully compressed. After the end of the ramp, the roller is free and the Force spring transfers its potential energy into kinetic energy for the hammer and the actuator (stage d). The hammer hits the housing mass and the whole system is pushed deeper into the soil. At the same time the actuator mass is sliding upwards and compresses the Brake spring (stage e). The Brake spring unloads as well and accelerates the actuator together with the hammer towards the tip. A second, smaller hit occurs and pushes the Mole another step deeper into the soil (stage f). After that, the masses and springs are in their starting position for the next cycle. The whole cycle takes place during one revolution of the drive shaft. For the HP³-Mole this cycle takes about 3 seconds, where the stroke part lasts for approx. 0.1 seconds.

As the Mole is a closed system with no force from the outside (except for gravity), there should be hardly any movement of the Mole. But as the fast movement of the housing mass overcomes the static friction and the slow backwards movement of the actuator doesn't, the Mole can penetrate the soil. It doesn't even needs the help of gravity as it can also penetrate in horizontal direction.

1.3. Moles - State of the art

There are various developed Moles or Mole-related instruments so far. The common base of these systems is that they contain an internal hammering mechanism that allows penetration into the subsurface of its target.

1.3.1. PLUTO-Mole

PLUTO (PLanetary Underground TOol) is a Mole sampling mechanism that was part of Beagle 2 on the MarsExpress mission of ESA. It is one of the predecessors of HP³ and was also developed by DLR. In addition to the hammering mechanism PLUTO had a sample chamber

inside the tip. It was possible to open it in the designated depth, take the sample and return to the surface. The return was established with less powerful backwards strokes assisted with a winch on the surface. As Beagle 2 failed to operate on Mars, PLUTO wasn't penetrating Mars in the end. Fig. 1.6 shows the PLUTO-Mole [RD 10].

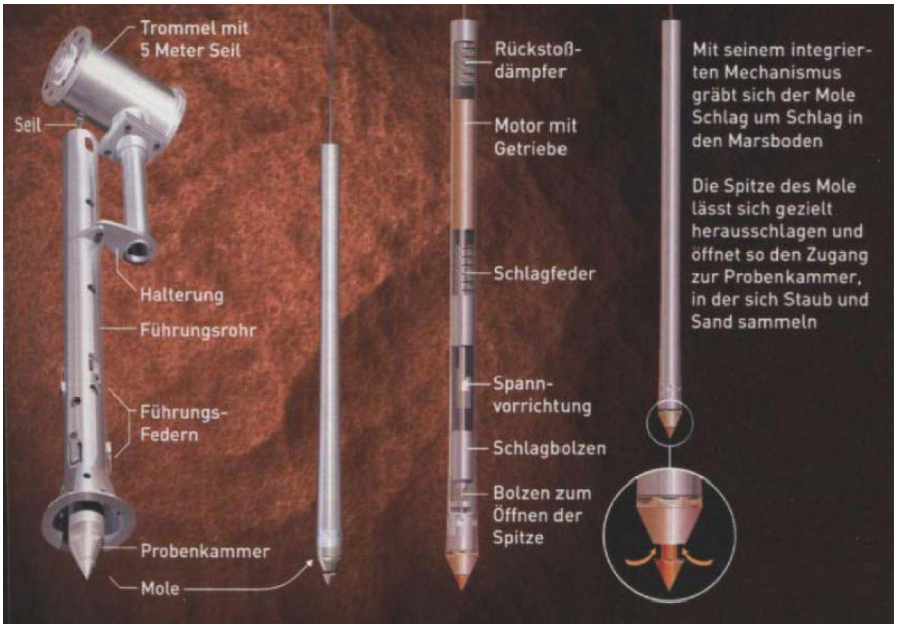

Fig. 1.6: PLUTO-Mole [RD 10]

1.3.2. MUPUS

MUPUS (Multi-Purpose Sensors for Surface and Sub-Surface Science) is a Mole-like instrument on the Philae-Lander of Rosetta. The basic functionality is comparable to other Moles and it is used for several different measurements on 67P/Churyumov-Gerasimenko. In one point it is fundamental different compared to other Moles: The hammering mechanism stays above the surface and only an instrumented rod will be penetrating the comet. For this reason the hammering mechanism is significant bigger than on other Moles. The rod is instrumented with sensors to determine the heat flow of the comet. MUPUS will start operating towards the end of 2014 [RD 4].

1.3.3. MMUM

The Moon/Mars Underground Mole (MMUM) is a concept of NASA for an instrumented Mole which should also take a soil sample. With a diameter of 40 mm, a length of 600 mm and weight of approx. 2 kg, it is bigger as other Moles that actually penetrate the soil. The planned instruments inside the MMUM are a Raman-spectrometer and temperature sensors [RD 17].

1.3.4. KRET

KRET (Polish for mole) is a Mole developed by the Space Research Centre of the Polish Academy of Science (CRS PAS). The hammering mechanism is more complex as in the HP³-

Mole. The displacement of the Force spring is taken place during several revolutions of the drive shaft and the hammer is hold by a latch during this phase. This allows a bigger displacement of the spring and a bigger energy output per stroke. Hence the time for each cycle is longer. CRS PAS also performed some tests with regard to different tip shapes and their influence on the penetration performance. The scientific use of this Mole is in characterizing soil parameters. During penetration the output energy is known and with defined soil a calibration for the digging performance and its relation to soil parameters can be established. When the KRET is penetrating another soil, it is possible to derive some parameters with this calibration [RD 9].

1.3.5. Cryo-Mole / MMS-Mole

The Cryo-Mole and the MMS-Mole are two concepts developed by the DLR, which are closely related to the HP³-Mole.

The Cryo-Mole is a combination of a Mole and a melting probe. Additional to the internal hammering mechanism it has external heating foils attached. With this combination it is possible to penetrate into subsurfaces inaccessible for pure Moles or pure melting probes. These are areas of soil with ice enclosures or ice with contaminations in it. Examples for this are the pole regions of Mars or ice in Antarctica. If a pure Mole hits an ice enclosure it will probably be stuck or will be slowed down immensely, depending on the size of the ice. A heat probe in dirty ice can melt away most of the ice, but as it proceeds deeper a soil layer around the tip will assemble. In both cases the other instrument would be useful as well.

The MMS-Mole (micro-mass spectrometer-Mole) is a Mole with an integrated mass spectrometer developed by the Open University in Milton Keanes (UK). It is an bigger Mole in diameter to fit in the instrument and with some specification to allow the operation of the mass spectrometer. This Mole is big enough to store other small instruments, e.g. a Radon detector developed by the French “Institut de Recherche en Astrophysique et Planétologie”. Therefor the MMS-Mole has a modular setup to allow simple changes to the design without remodeling the whole system.

1.4. Motivation

The hammering mechanism of the HP³-Mole is unchanged since a few models. A better performance of the Mole while restricted by the same requirements as before can increase the possibility to reach the maximum depth of 5 meter. Therefor several changes in the design are considered and estimated with the effort of implementing them. Even if the changes will not be used for the InSight mission, an evolution of the HP³-Mole can increase the chance for the use of this system in later missions. To enable these options, this thesis is handling the analytical calculation of improvements, their implementation in the system and their testing and comparison with the theory.

2. Mole theory

In the following chapter the basic equations for one hammering cycle are described. They are used to calculate the actual and possible performances of the Mole and to compare these with another.

2.1. Displacement of the Force spring

The first part of a hammering cycle is the displacement of the Force spring. In this phase the Roller is rotated with the Drive shaft. With the driving force F_a it is pushed against the Cylindrical cam. The Cylindrical cam is then pressed against the Force spring with the Force spring force F_f. Therefor the Force spring is compressed. Between the Roller and the Cylindrical cam the normal force F_n is at work. The friction for the rolling Roller on the Cylindrical cam is then $\mu_{ro} * F_n$ with the coefficient of friction for rolling $\mu_{ro.}$ The occurring forces on the Roller are shown in Fig. 2.1.

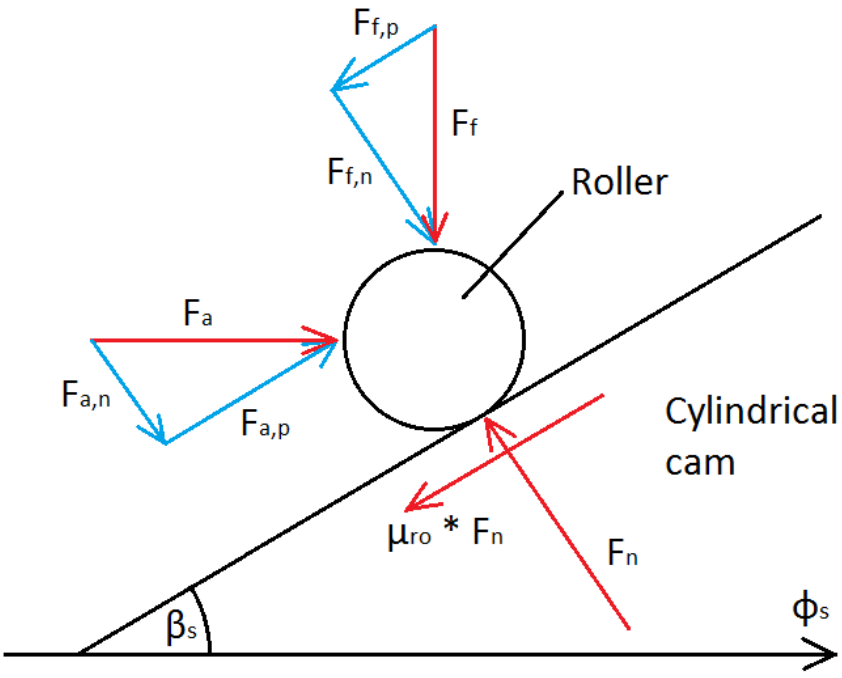

Fig. 2.1: Forces on the Roller

The driving and Force spring forces are split in normal and parallel parts. The equations of equilibrium are:

$$0 = F_{a,n} + F_{f,n} - F_n \tag{2.1}$$

$$0 = F_{a,p} - F_{f,p} - \mu_{ro} \cdot F_n \tag{2.2}$$

With the gradient angle of the Cylindrical cam β_s the normal and parallel forces can be replaced with the original forces:

$$F_{a,n} = F_a \cdot \sin \beta_s \tag{2.3}$$

$$F_{a,p} = F_a \cdot \cos \beta_s \tag{2.4}$$

$$F_{f,n} = F_f \cdot \cos \beta_s \tag{2.5}$$

$$F_{f,p} = F_f \cdot \sin \beta_s \tag{2.6}$$

Solving this system of equations for F_a and put in the slope of the Cylindrical cam s'

$$s' = \tan \beta_s \tag{2.7}$$

gives

$$F_a = F_f \cdot \frac{\mu_{ro} + s'}{1 - \mu_{ro} \cdot s'} \tag{2.8}$$

The drive torque of the Motor and Gear box is needed for two parts. One part is the driving force. It has the lever arm r_m, which is the mid radius of the Cylindrical cam:

$$r_m = \frac{r_a + r_i}{2} \tag{2.9}$$

with the outer radius r_a and the inner radius r_i of the Cylindrical cam. The second part is used for the friction force μ_{ru}*F_{wr} between Roller and Hammer (see Fig. 2.2), with the coefficient of friction for slipping μ_{ru}. Its lever arm is the outer radius of the Roller r_{ar}.

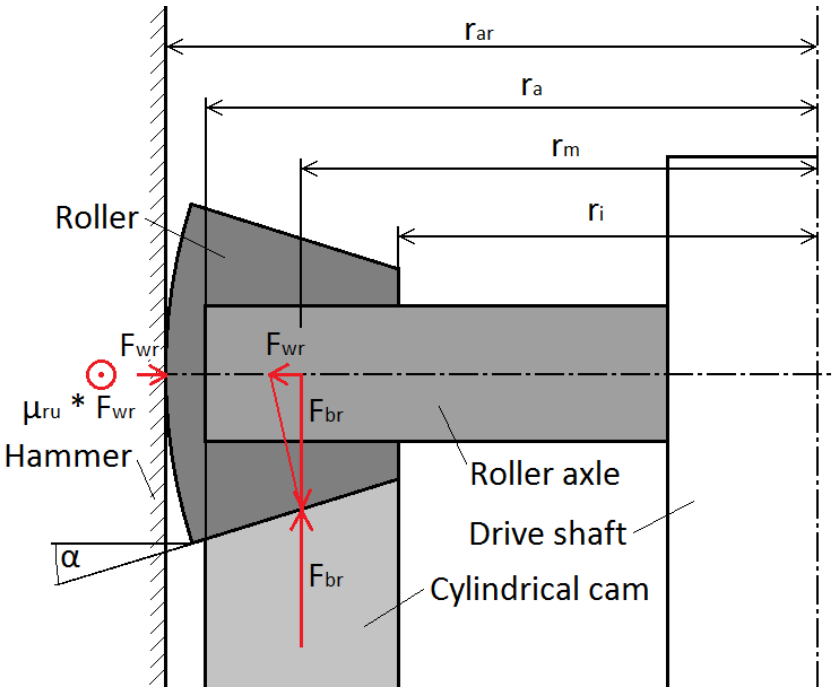

Fig. 2.2: Forces between Cylindrical cam, Roller and Hammer

The occurring loads are multiplied with a safety factor S_m. This results in the formula for the driving torque M_a, which has to be always lower than the maximum driving torque available:

$$M_a = S_m \cdot (F_a \cdot r_m + \mu_{ru} \cdot F_{wr} \cdot r_{ar}) \leq M_{a,max} \tag{2.10}$$

On the Roller appears the Roller load force F_{br} which is composed of the driving force and the Force spring force:

$$F_{br} = \sqrt{F_a^2 + F_f^2} \tag{2.11}$$

As seen in Fig. 2.2 the Roller side force F_{wr} can then be calculated with:

$$F_{wr} = \tan \alpha \cdot F_{br} \tag{2.12}$$

whereas α is the inclination of the Roller path. Inserting the equations (2.8), (2.11) and (2.12) in (2.10) provides

$$M_a = S_m \cdot F_f \cdot \left(\frac{\mu_{ro} + s'}{1 - \mu_{ro} \cdot s'} \cdot r_m + \mu_{ru} \cdot \tan \alpha \cdot \sqrt{\left(\frac{\mu_{ro} + s'}{1 - \mu_{ro} \cdot s'} \right)^2 + 1} \cdot r_{ar} \right) \tag{2.13}$$

The Force spring force F_f can be computed by

$$F_f = s \cdot c_f + k_f \tag{2.14}$$

$$k_f = (l_{f,u} - l_{f,p}) \cdot c_f + F_{r,12} + m_1 \cdot g \cdot \sin \chi \approx const. \tag{2.15}$$

where s is the height of the Cylindrical cam, c_f is the spring rate for the Force spring. The Force spring force constant k_f contains the force due to the precompressed Force Spring by $l_{f,u} - l_{f,p}$, the force of friction between the hammer and the Hammer support structure $F_{r,12}$ and the gravitation of the hammer with the inclination angle χ (see Fig. 2.3). For the comparisons in this thesis χ is set to 90°, which also provides the highest loads. As shown in 2.2 the mass of the hammer is not fixed and therefor is k_f not a real constant, but it is as a good approach since:

$$(l_{f,u} - l_{f,p}) \cdot c_f \gg m_1 \cdot g \cdot \sin \chi \tag{2.16}$$

For example with values for the Breadboard-model: 23.0 N >> 1.0 N. With the Force spring force (2.14) the equation (2.13) can be converted in the differential equation for the driving torque:

$$M_a = S_m \cdot (s \cdot c_f + k_f) \cdot \left(\frac{\mu_{ro} + s'}{1 - \mu_{ro} \cdot s'} \cdot r_m + \mu_{ru} \cdot \tan \alpha \sqrt{\left(\frac{\mu_{ro} + s'}{1 - \mu_{ro} \cdot s'} \right)^2 + 1} \cdot r_{ar} \right) \tag{2.17}$$

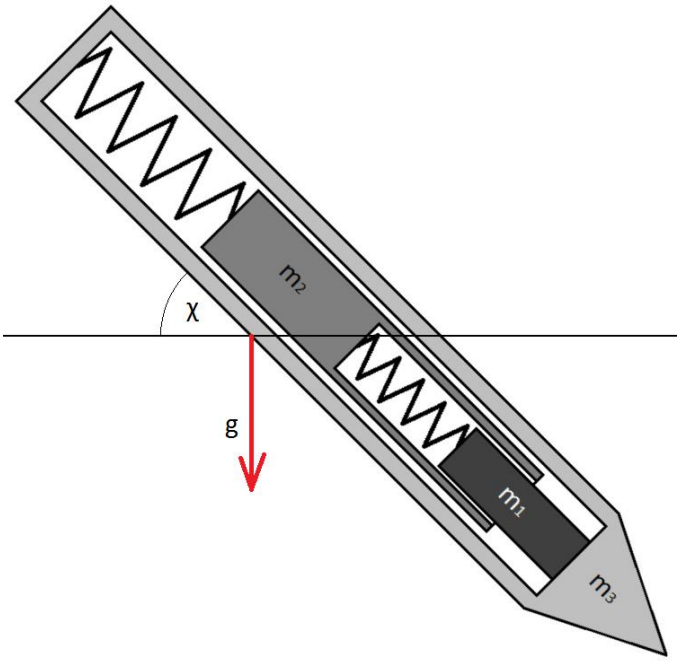

Fig. 2.3: Inclination χ of the Mole

The height s is a function of the rotational angle of the Cylindrical cam ϕ_s. In all following considerations the slope of the Cylindrical cam is not constant and can change its value with the rotational angle ϕ_s, too. The remaining parameters of (2.16) are geometrical values, coefficients of friction or other constants. Hence the driving torque is a function of s and s', which change with ϕ_s:

$$M_a = f\left(s(\varphi_s), s'(\varphi_s)\right) \tag{2.18}$$

For the equations of the strokes the length of the compressed Force spring $l_{f,c}$ is needed. This can be calculated with the maximum height of the Cylindrical cam s_2 and the precompressed length for the Force spring $l_{f,p}$:

$$l_{f,c} = l_{f,p} - s_2 \tag{2.19}$$

$$s_2 = s\left(\varphi_{s,2}\right) \tag{2.20}$$

$$s = \frac{M_a(\varphi_s)}{S_m \cdot \left(\frac{\mu_{ro} + s'(\varphi_s)}{1 - \mu_{ro} \cdot s'(\varphi_s)} \cdot r_m + \mu_{ru} \cdot \tan\alpha \cdot \sqrt{\left(\frac{\mu_{ro} + s'(\varphi_s)}{1 - \mu_{ro} \cdot s'(\varphi_s)} \right)^2 + 1} \cdot r_{ar} \right) \cdot c_f - \frac{k_f}{c_f}} \tag{2.21}$$

with $\phi_{s,2}$ the rotational angle at the end of the Cylindrical cam.

2.2. Model for energy transfer

In the following passage the model for the energy transfer for the primary and secondary stroke is discussed. After the displacement of the Force spring it stores the Force spring energy E_f, which is the initial energy for the model:

$$E_f = \frac{1}{2} \cdot c_f \cdot \left(\left(l_{f,u} - l_{f,c} \right)^2 - \left(l_{f,u} - l_{f,p} \right)^2 \right) \tag{2.22}$$

with the uncompressed length $l_{f,u}$ and the precompressed length $l_{f,p}$ of the Force spring. After the release of the Roller the Force spring energy splits into two kinetic energies for the hammer mass $E_{1,kin}$ and the actuator mass $E_{2,kin}$ (compare with Fig. 2.4):

$$E_{1,kin} = \frac{E_f}{1 + \frac{m_1}{m_2}} = \frac{1}{2} \cdot m_1 \cdot v_1^2 \tag{2.23}$$

$$E_{2,kin} = \frac{E_f}{1 + \frac{m_2}{m_1}} = \frac{1}{2} \cdot m_2 \cdot v_2^2 \tag{2.24}$$

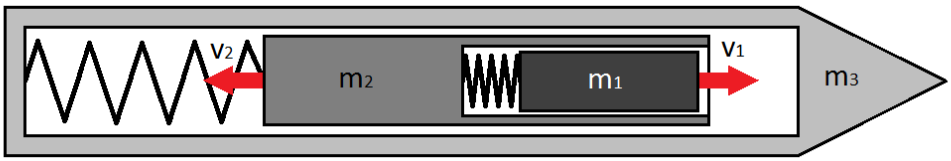

Fig. 2.4: Velocities of m_1 and m_2 prior to the primary stroke

The velocity of the hammer mass before the primary stroke is

$$v_1 = \sqrt{\frac{2 \cdot E_{1,kin}}{m_1}} \tag{2.25}$$

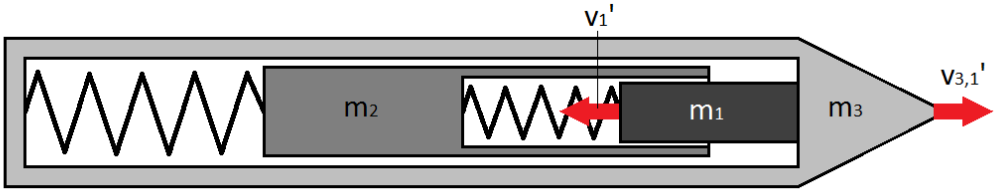

Fig. 2.5: Velocities of m_1 and m_3 after the primary stroke

After the primary stroke the resulting velocities of the hammer mass and the housing mass shown in Fig. 2.5 are calculated (compared to [RD 1]) with:

$$v_1' = \frac{m_1 \cdot v_1 + m_3 \cdot v_{3,1} - m_3 \cdot \left(v_1 - v_{3,1} \right) \cdot k_s}{m_1 + m_3} \tag{2.26}$$

$$v'_{3,1} = \frac{m_1 \cdot v_1 + m_3 \cdot v_{3,1} + m_1 \cdot (v_1 - v_{3,1}) \cdot k_s}{m_1 + m_3} \tag{2.27}$$

The kinetic energy of the hammer mass is divided into the kinetic energies after the stroke for the hammer mass $E_{1,kin,p}$ and for the housing mass $E_{3,kin,1}$ as well as the dissipative energy $E_{1,diss}$:

$$E_{1,diss} = \frac{m_1 \cdot m_3 \cdot v_1^2 \cdot (1 - k_s^2)}{2 \cdot (m_1 + m_3)} \tag{2.28}$$

$$E_{1,kin,p} = \frac{1}{2} \cdot m_1 \cdot \left(\frac{m_1 \cdot v_1 - m_3 \cdot v_1 \cdot k_s}{m_1 + m_3} \right)^2 \tag{2.29}$$

$$E_{3,kin,1} = E_{1,kin} - E_{1,diss} - E_{1,kin,p} \tag{2.30}$$

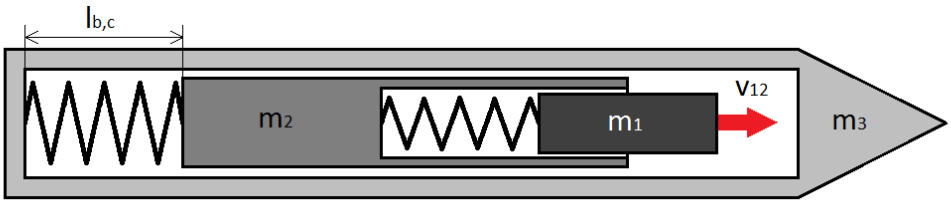

Fig. 2.6: Velocity of m_1 and m_2 prior to the secondary stroke and compressed length of the Brake spring

For the secondary stroke the actuator mass with its kinetic energy $E_{2,kin}$ is compressing the Brake spring. The compressed length of the Brake spring $l_{b,c}$ (see in Fig. 2.6) can be computed with:

$$E_{2,kin} = \frac{1}{2} \cdot c_b \cdot \left((l^*_{b,u} - l_{b,c})^2 - (l^*_{b,u} - l_{b,p})^2 \right) \tag{2.31}$$

$$l_{b,c} = l^*_{b,u} - \sqrt{(l^*_{b,u} - l_{b,p})^2 + \frac{2 \cdot E_{2,kin}}{c_b}} \tag{2.32}$$

with the spring rate c_b and the precompressed length $l_{b,p}$ of the Brake spring. Due to additional forces on the actuator mass a virtual uncompressed length $l_{b,u}^*$ is used instead of the uncompressed length $l_{b,u}$ to simplify (2.29). It is composed of the uncompressed length, a part for the gravitation on hammer and actuator mass and a part for the friction force between the actuator and the housing mass $F_{r,23}$:

$$l^*_{b,u} = l_{b,u} + \frac{(m_1 + m_2) \cdot g \cdot \sin \chi}{c_b} + \frac{F_{r,23}}{c_b} \tag{2.33}$$

During the displacement and relaxing of the Brake spring the actuator mass is affected by $F_{r,23}$ for twice the difference of the precompressed and compressed length of the Brake spring:

$$E_{12,kin} = E_{2,kin} - 2 \cdot F_{r,23} \cdot (l_{b,p} - l_{b,c}) \tag{2.34}$$

The velocity of the hammer and actuator mass before the secondary stroke v_{12} (Fig. 2.6) is calculated from the kinetic energy of those masses $E_{12,kin}$:

$$v_{12} = \sqrt{\frac{2 \cdot E_{12,kin}}{m_1 + m_2}} \tag{2.35}$$

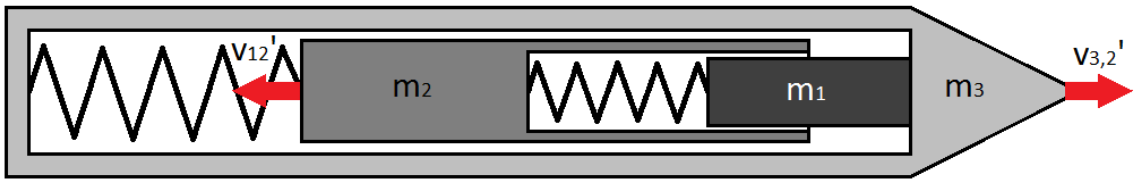

Fig. 2.7: Velocities for m_1 and m_2 as well as m_3 after the secondary stroke

Equally to the primary stroke the velocities of the hammer and actuator mass v_{12}' and the housing mass $v_{3,2}$' (Fig. 2.7) are calculated with:

$$v'_{12} = \frac{(m_1 + m_2) \cdot v_{12} + m_3 \cdot v_{3,2} - m_3 \cdot (v_{12} - v_{3,2}) \cdot k_s}{m_1 + m_2 + m_3} \tag{2.36}$$

$$v'_{3,2} = \frac{(m_1 + m_2) \cdot v_{12} + m_3 \cdot v_{3,2} + (m_1 + m_2) \cdot (v_{12} - v_{3,2}) \cdot k_s}{m_1 + m_2 + m_3} \tag{2.37}$$

The secondary stroke results in the kinetic energies for the hammer and actuator mass $E_{12,kin,p}$ and for the housing mass $E_{3,kin,2}$ after the stroke and results also in the dissipative energy of the stroke $E_{12,diss}$:

$$E_{12,diss} = \frac{m_3 \cdot (m_1 + m_2) \cdot v_{12}^2 \cdot (1 - k_s^2)}{2 \cdot (m_1 + m_2 + m_3)} \tag{2.38}$$

$$E_{12,kin,p} = \frac{1}{2} \cdot (m_1 + m_2) \cdot \left(\frac{(m_1 + m_2) \cdot v_{12} - m_3 \cdot v_{12} \cdot k_s}{m_1 + m_2 + m_3} \right)^2 \tag{2.39}$$

$$E_{3,kin,2} = E_{12,kin} - E_{12,diss} - E_{12,kin,p} \tag{2.40}$$

The kinetic energies of the housing $E_{3,kin,1}$ in (2.27) and $E_{3,kin,2}$ in (2.35) displace the Mole dependent of the properties of the surrounded soil. For further studies the totally kinetic energy $E_{3,kin}$ for one hammering cycle is computed with:

$$E_{3,kin} = E_{3,kin,1} + E_{3,kin,2} \tag{2.41}$$

The variables that influence this energy are the spring rates c_b and c_f and the three masses m_1, m_2 and m_3. Furthermore the maximum height of the Cylindrical cam s_2, which is the

same as the displacement length of the Force spring, affects the kinetic energy of the housing (this was shown in 2.1):

$$E_{3,kin} = f(c_b, c_f, m_1, m_2, m_3, s_2) \tag{2.42}$$

This set of parameters builds the baseline for investigating the possibilities of improvements to the Hammering mechanism in chapter 3.

2.3. Implementation in Mole-simulation

To evaluate the influence of design changes on a Mole model, the department of exploration systems developed a simulation for Moles [RD 8]. It was written in MATLAB with Simulink. All the necessary data can be filled in the initial file, such as masses, overall dimensions and spring properties. As results the simulation outputs the needed current and torque of the motor/gear box combination during the displacement phase, the energies of the three masses during the strokes phase and the penetration depth over time. In Fig. 2.8 the torque for the motor during displacement of the Force spring over one revolution of the Drive Shaft is displayed. This example represents the shape of the Cylindrical cam of the PT-Mole design. The maximum torque of the motor and gear box is marked with the horizontal lines. The full output of the simulation shows Appendix A.

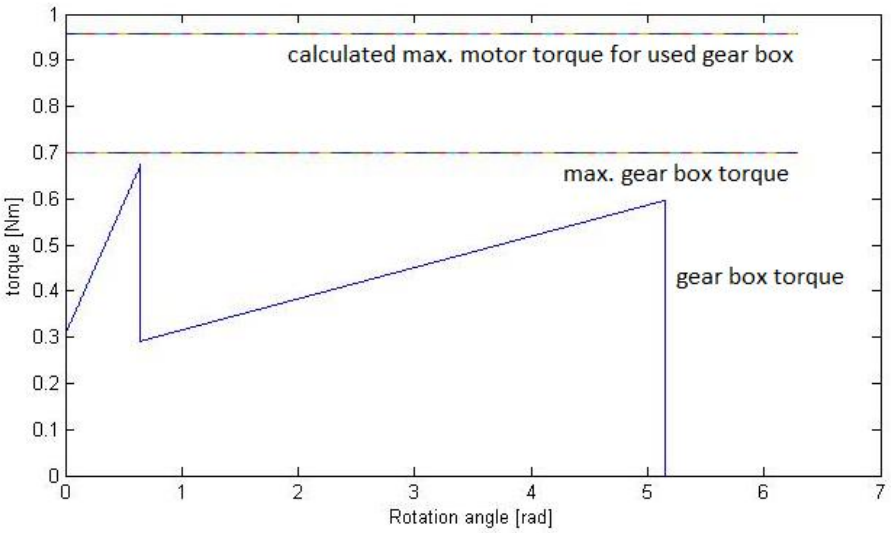

Fig. 2.8: Torque on gear box for PT-Mole

To get to those results, the simulation used a similar set of equations like those in 2.1 and 2.2 in the past. During this thesis the equations were enhanced to include all the additional parameters that were stated in 2.1 and 2.2. These were more detailed coefficients of friction and the safety factor σ_m. In the previous version of the simulation, the shape of the Cylindrical cam could only described as up to three discrete slopes in three specified sections. This part of the simulation was changed to allow variable slopes. Therefor it is now possible to use functions and their derivatives for the shape and change parameters in them.

The part for the penetration rate uses the energy of the Outer Hull, the dimensions of the Mole and a soil model to compute the penetrated distance per stroke. As some of the soil parameters are dependent of the depth, the simulation uses Simulink to calculate the penetration depth over time. For most of the issues of this thesis this part of the simulation is sufficient and wasn't changed. The soil model reaches its limits for the different Tip shapes. That will be treated in 4.2.

3. Parameter analysis

Like it was shown in 2.2 the energy transferred to the housing is correlated to several parameters of the system. In the following chapter these parameters will be divided in three groups: the masses, the Force spring displacement and the spring rates.

The baseline that provides the remaining or yet unchanged parameters is the Breadboard-model of the HP³-Mole. Tab. 3.1 shows an excerpt of this parameter set.

Parameter	BB-Mole
Spring rate Force spring c_f	11.6 N/mm
Uncompressed length Force spring $l_{f,u}$	43.98 mm
Precompressed length Force spring $l_{f,p}$	42 mm
Compressed length Force spring $l_{f,c}$	35 mm
Spring rate Brake spring c_b	0.222 N/mm
Uncompressed length Brake spring $l_{b,u}$	70 mm
Precompressed length Brake spring $l_{b,p}$	38 mm
Hammer mass m_1	105 g
Actuator mass m_2	230 g
Housing mass m_3	552 g
Coefficient of restitution k_s	0.67
Angle of slope Cylindrical cam $\beta_{s,1}$	33.21°
Angle of slope Cylindrical cam $\beta_{s,2}$	10.24°
Rotational angle Cylindrical cam $\phi_{s,1}$	37.09°
Rotational angle Cylindrical cam $\phi_{s,2}$	295.00°
Coefficient of friction for rolling μ_{ro}	0.2
Coefficient of friction for slipping μ_{ru}	0.15
Safety margin for torque σ_m	2

Tab. 3.1: Parameters of BB-Mole

3.1. Mass ratio

The optimized masses are highly depended on each other. The change of one mass varies the optimal value for another mass. Therefor all three masses will be set into a ratio and the optimal ratio will be investigated in this thesis. The only effect of the masses on the spring displacement phase is the gravitational contribution of the hammer mass. Compared to the other occurring forces this part has a minor effect (see 2.1). Hence the main work for determining the mass ratio treats the energy transfer model of 2.2.

3.1.1. Prototype-Mole design

Due to the project schedule the design of the Prototype-model of the HP³-Mole should use the same Hammering mechanism as for the Breadboard-Mole. For the Prototype-Mole the mass of the housing is changing. Therefor the masses are compared to the Breadboard-Mole first and the potential in changing the housing mass is investigated. A complete variation of all masses is investigated in 3.1.2.

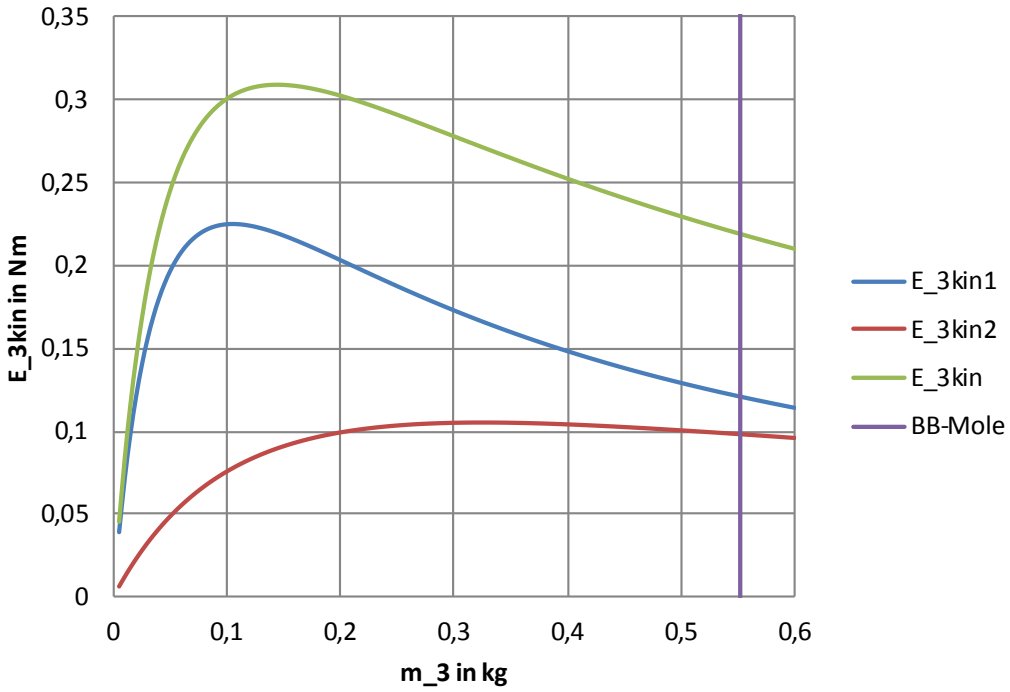

Fig. 3.1: Optimization of the housing mass for the PT-Mole

Using the parameters of the BB-Mole listed prior, the curve for the kinetic energy of the housing mass calculates as shown in Fig. 3.1. In this case the housing mass was varied between 0 and 0.6 kg in 0.005 kg steps. Reducing the mass of the housing from 0.552 kg to approx. 0.145 kg would result in a significant improvement. With an overall kinetic energy of both strokes ($E_{3,kin}$) of 0.303 Nm, this change would provide an enhancement of 38.4 % (BB-Mole: $E_{3,kin}$ = 0.219 Nm). In terms of the Mole theory the scientific instruments TEM-A and STATIL and the internal electronics of the Mole are part of the housing mass. Therefor it is the task for the PT-design to implement the instruments and electronics and reduce the housing mass to 0.145 kg. This is further described in 4.1.1.

3.1.2. Complete variation of mass ratio

In the following part the mass ratio is determined which uses the same total mass of the system as the PT-design and maximizes the kinetic energy of the housing. The total mass of the PT-Mole is 0.52 kg with a realized housing mass of 0.195 kg. If the total mass is not fixed, the kinetic energy of the housing can be increased more and more with a raising total mass. But as this system is part of a flight mission the mass should be low.

Varying the three masses concludes in the following figures:

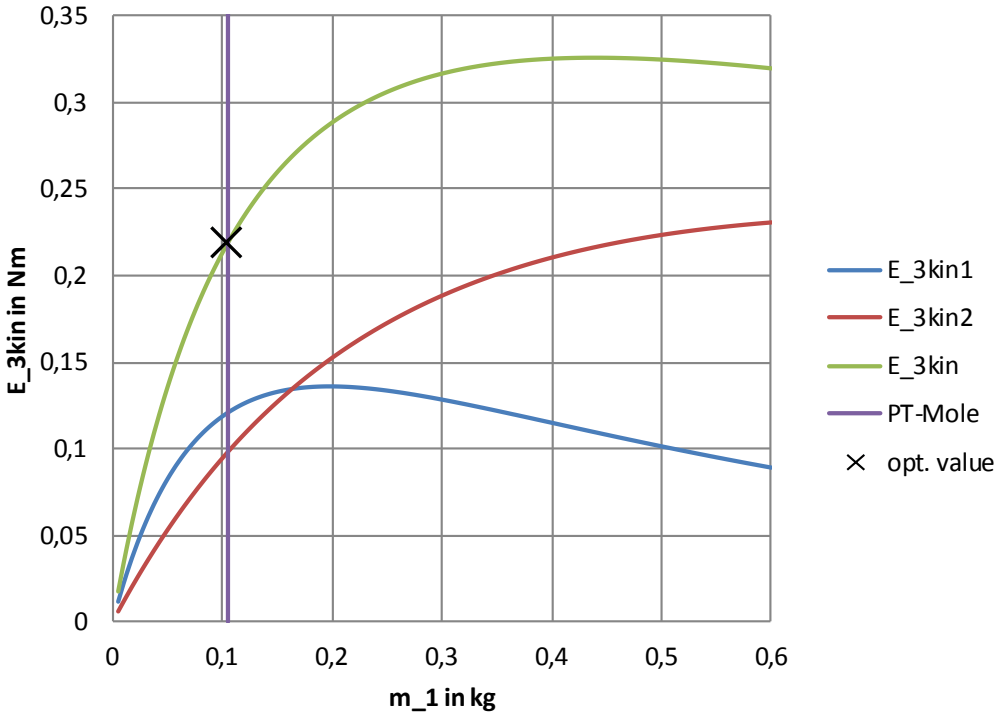

Fig. 3.2: Theoretical optimization of mass ratio – hammer mass

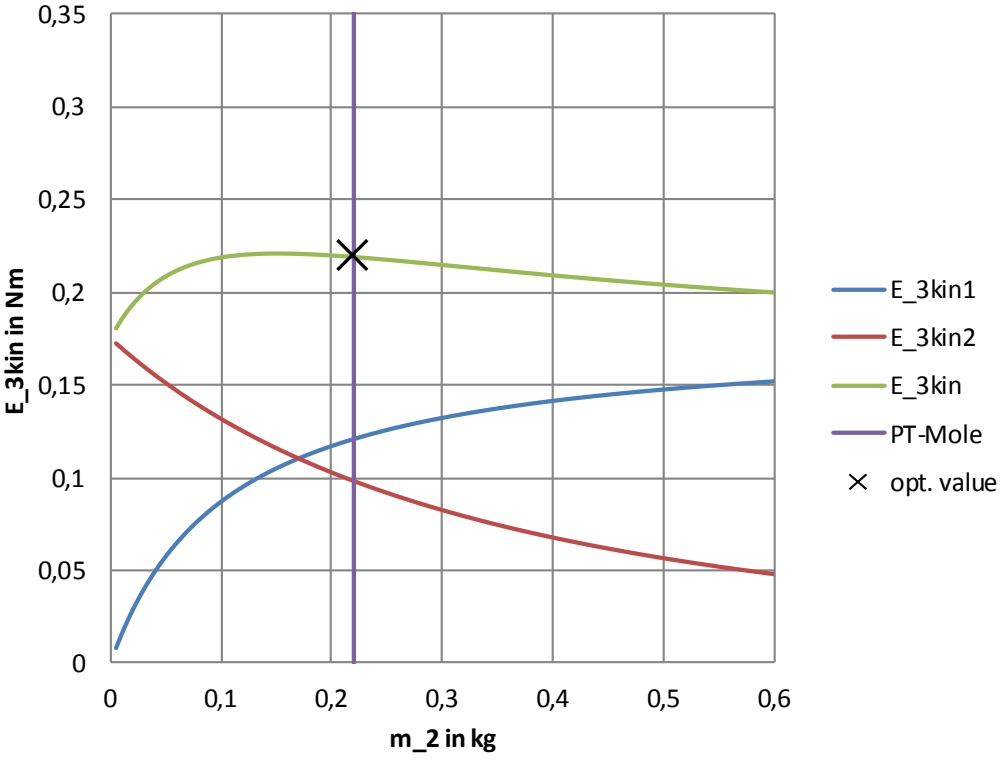

Fig. 3.3: Theoretical optimization of mass ratio – actuator mass

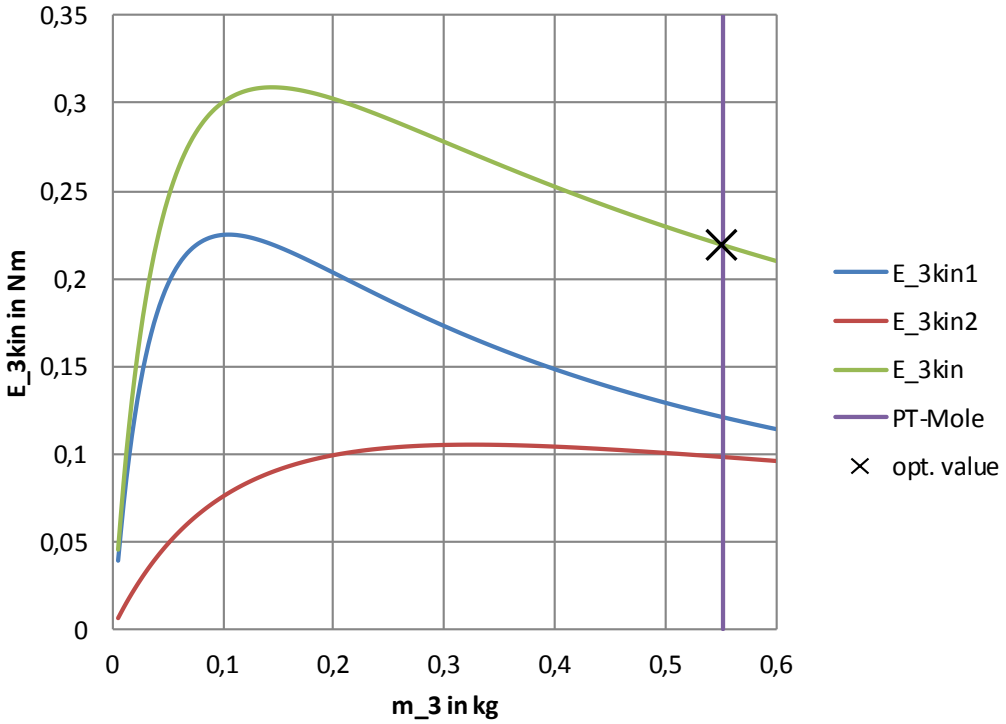

Fig. 3.4: Theoretical optimization of mass ratio – housing mass

The optimal values for the masses are 0.215 kg for m_1, 0.050 kg for m_2 and 0.255 kg for m_3. This is a ratio of 4.3/1/5.1 ($m_1/m_2/m_3$). For this mass ratio the kinetic energy is 0.327 Nm, which would be an improvement of 7.9 % compared to the PT-Mole and 49.3 % compared to the BB-Mole. However, the realization of the actuator mass is not possible. The main part of this assembly is the motor and the gear box. With a weight of the used motor gear box-unit in the BB-Mole and PT-Mole of 0.095 kg the aimed-at mass is already exceeded. The other parts of this assembly, which partly experience high loads during the hammering process, shouldn't be built too light weight. Additionally the whole principle of hammering would be changed for a design with these values. In Fig. 3.2, Fig. 3.3 and Fig. 3.4 it is shown that the kinetic energy of the first stroke is considerable lower than the second stroke. That results in a change of purposes for the springs and masses. The displacement of the Force spring and the first stroke by the hammer is only used for the displacement of the Brake spring. Then the Brake spring would fulfill the work of the Force spring and accelerate the actuator and hammer towards the housing. This new hammering behavior would need to be checked with different models and additional tests to verify the model. This is neither the intention of the project nor of this thesis.

In another optimization the mass of the actuator will be fixed to the 0.220 kg of the BB-Mole. To ensure that the total mass is not increasing significant and the second stroke has a smaller share of the kinetic energy of the housing, the housing mass is set to the realized mass of the PT-design (0.195 kg). Therefor the only varying mass is the hammer:

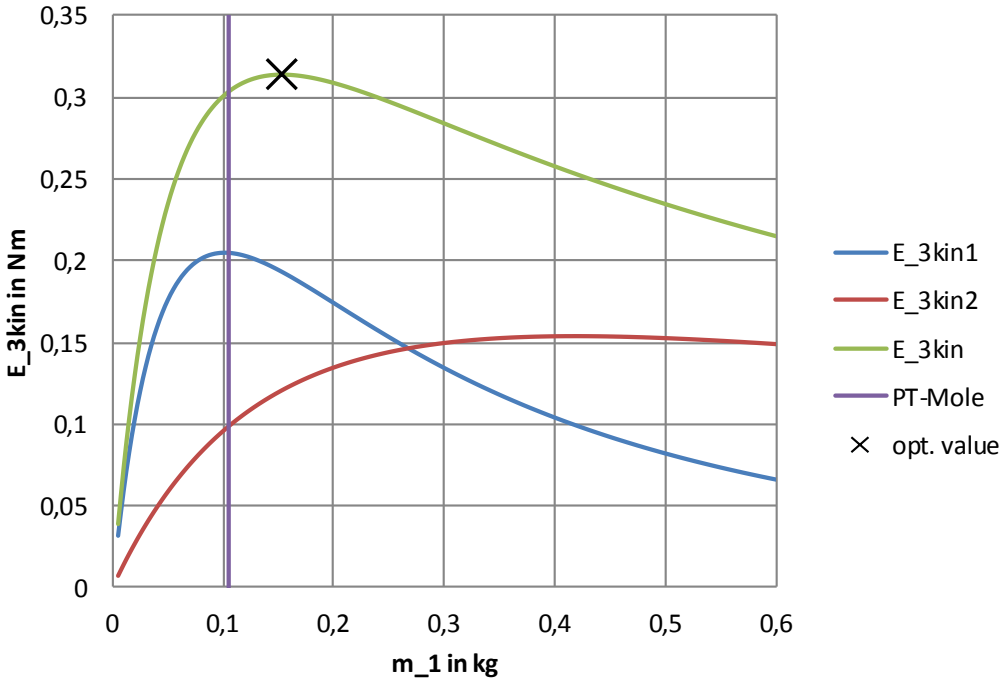

Fig. 3.5: Optimization of the hammer mass for restricted values for actuator and housing

Fig. 3.5 shows the optimal value of 0.155 kg for the hammer with the already set masses of the actuator and housing. The kinetic energy for this case is 0.314 Nm, an improvement of 3.6 % compared to the PT-Mole and 43.4 % to the BB-Mole. The mass ratio is 1/1.42/1.26 and the total mass is 0.570 kg.

3.2. Force spring displacement

In 2.1 the equation (2.21) for the spring displacement s with all influencing parameters was developed. This builds the base for the investigation of the optimization of the spring displacement:

$$s = \frac{M_a(\varphi_s)}{S_m \cdot \left(\frac{\mu_{ro} + s'(\varphi_s)}{1 - \mu_{ro} \cdot s'(\varphi_s)} \cdot r_m + \mu_{ru} \cdot \tan\alpha \cdot \sqrt{\left(\frac{\mu_{ro} + s'(\varphi_s)}{1 - \mu_{ro} \cdot s'(\varphi_s)} \right)^2 + 1} \cdot r_{ar} \right) \cdot c_f} - \frac{k_f}{c_f} \tag{3.1}$$

A bigger spring displacement increases the Force spring energy E_f. As seen in 2.2 this energy is the starting point for the energy transfer of the strokes and the kinetic energy of the housing is nearly proportional to it. Therefor the goal of this optimization is to increase the spring displacement to a maximum within the technical restrictions.

Some of the parameters are given by mission requirements (safety margin σ_m) or due to dimensional restrictions in the Mole design (mid radius of Cylindrical cam r_m and outer radius of Roller r_{ar}). The force constant of Force spring k_f is nearly untouched for the change of the hammer mass and has only a very small influence on the spring displacement. With k_f = 24.2 N for the BB-Mole (105 kg hammer) compared to k_f = 24.7 N of the 0.155 kg hammer the difference in the spring displacement results in 0.04 mm between the mentioned hammer masses. This would be within manufacturing tolerances. The Force spring rate c_f is one of the topics of 3.3 and is not treated here. The friction coefficients μ_{ro} and μ_{ru} would decrease the spring displacement when rising (compare with (3.1)). Therefor the coefficients need to be as small as possible. These are values which are influenced by the manufacturing process and the lubrication during operation.

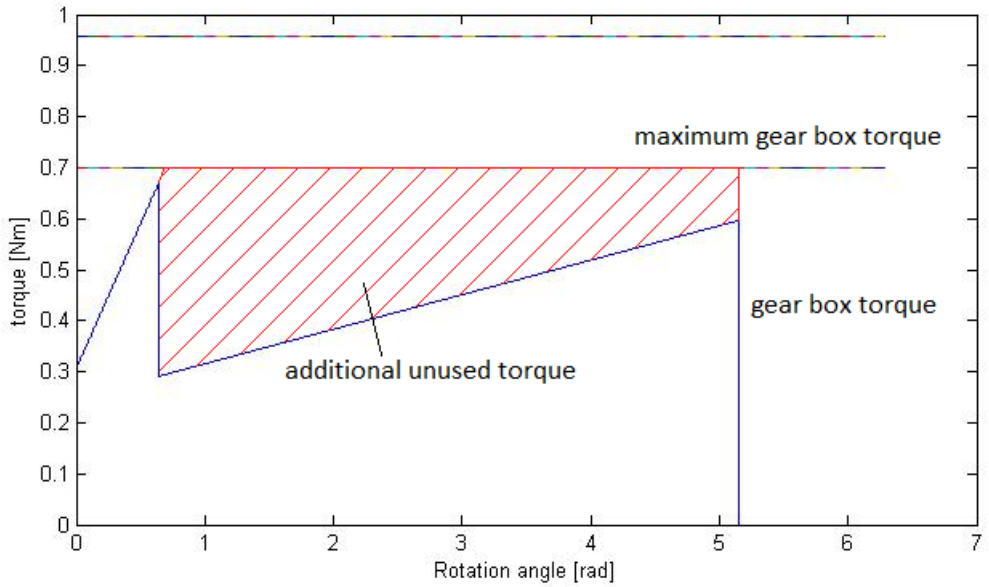

Fig. 3.6: Optimal used driving torque

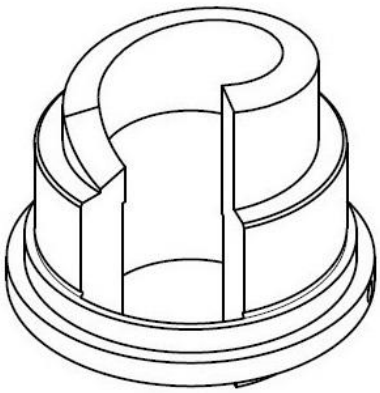

Fig. 3.7: Isometric view of the Cylindrical cam

In this section the driving torque M_a and the slope of the Cylindrical cam s' are the two variables to investigate. In Fig. 3.6 the torque profile of the motor gear box-unit is shown for one revolution of the Drive shaft of the PT-Mole. Fig. 3.7 depicts the Cylindrical cam. The red

hatched area shows the torque which could be used with the motor gear box-unit but is unused. This additional torque can be employed to reach a bigger spring displacement. To achieve this equation (3.1) is converted in a differential equation for the driving torque:

$$M_a(s, s') = S_m \cdot \left(s(\varphi_s) \cdot c_f + k_f\right) \cdot \left(\frac{\mu_{ro} + s'(\varphi_s)}{1 - \mu_{ro} \cdot s'(\varphi_s)} \cdot r_m + \mu_{ru} \cdot \sqrt{\left(\frac{\mu_{ro} + s'(\varphi_s)}{1 - \mu_{ro} \cdot s'(\varphi_s)} \right)^2 + 1} \cdot r_{ar} \right) \quad (3.2)$$

The requirements for this differential equation are the maximum torque of the gear box, the maximum rotational angle (kept the same as in the previous models) and the maximum slope. The equation is replaced by a constant slope that is chosen to be the maximum slope for the first section. It is the maximum slope that was used in the BB- and PT-Mole. In the past the Roller has shown that it can overcome this slope in practice.

The differential equation cannot be solved analytical. Therefor a self-written computer program by a colleague at DLR is used to solve this equation numerical. The result is a function of the height of the Cylindrical cam, which is equal to the spring displacement, depending on the rotational angle of the Drive shaft. Differentiate this function with respect to ϕ_s gives the slope of the Cylindrical cam. When applying the height function $s(\phi_s)$ and the slope function $s'(\phi_s)$ in (3.2) the torque progression should stay at a constant level for the numerical computed part. Yet the result wasn't a constant curve. Changing the approach to solve the differential equation numerical didn't give a better height function. Nevertheless implementing a numerical equation in the Mole-simulation and in the CAD-model would be quiet complicated. A numerical solution is also very impractical as for every changing parameter a new solution has to be found. Therefor several approaches with different functions were performed.

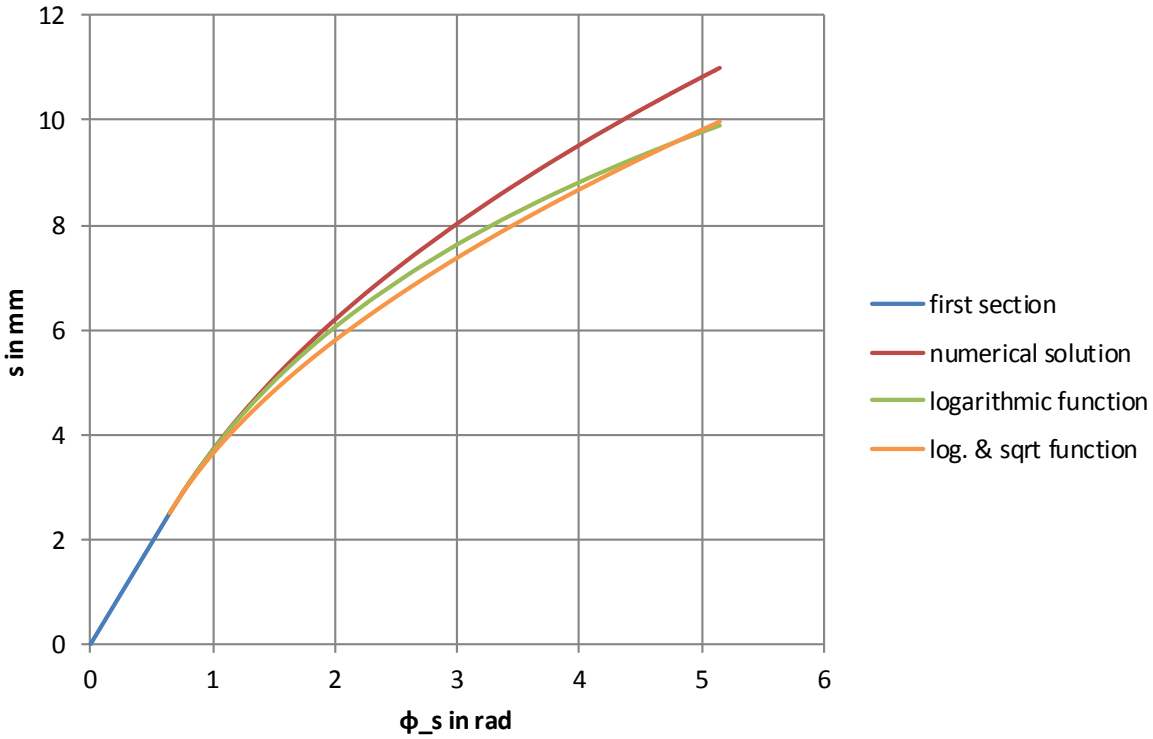

Fig. 3.8: Different approaches for optimized shape of Cylindrical cam

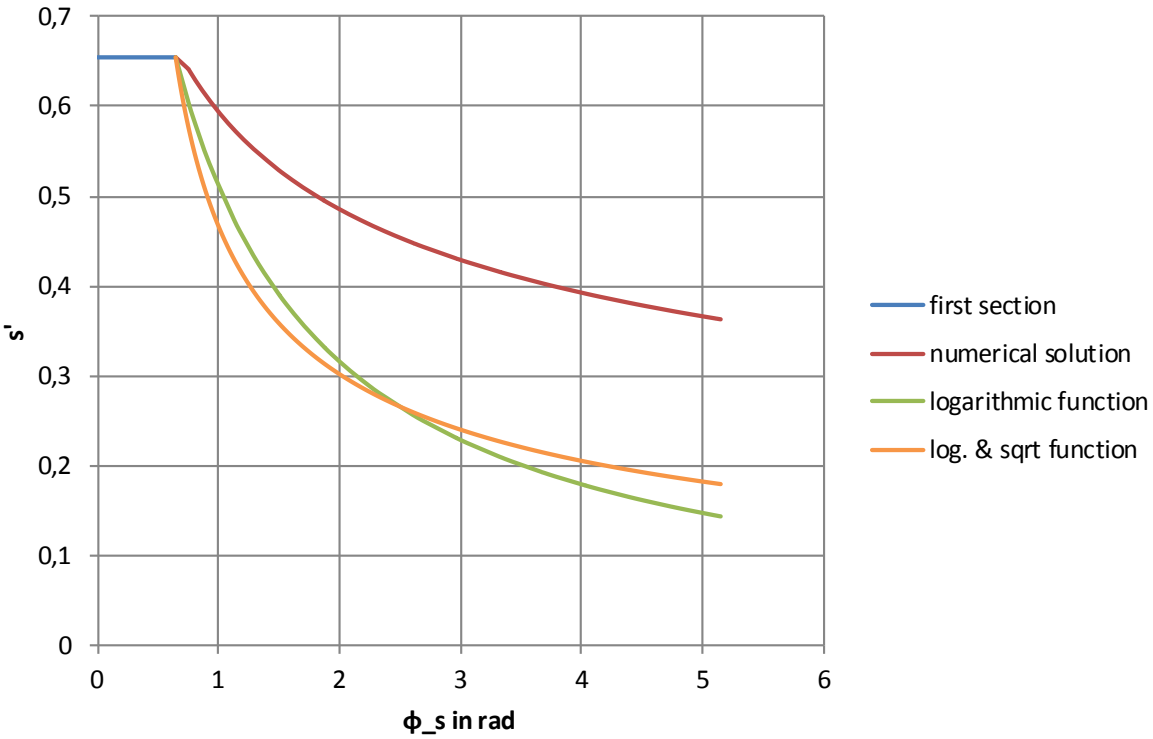

Fig. 3.9: Different approaches for optimized slope of Cylindrical cam

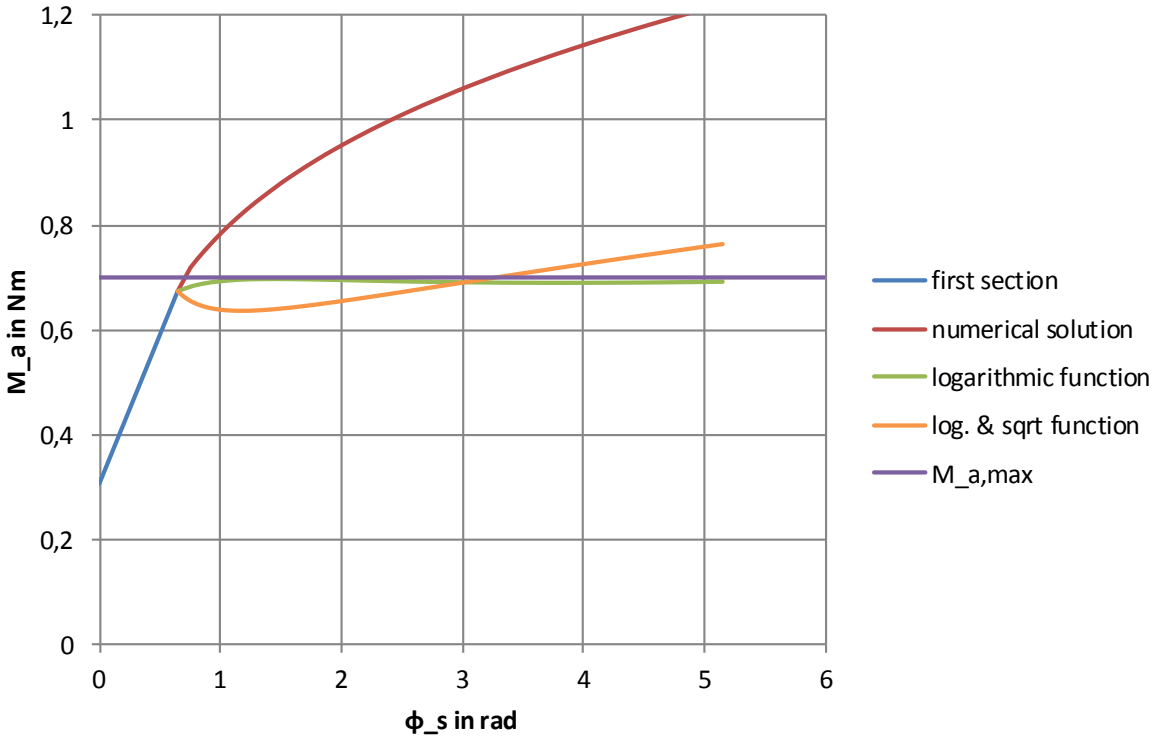

Fig. 3.10: Different approaches for optimized torque of gear box

Simplifying equation (3.2) suggested a square root function for the first approach. However, the graph of the torque was far too high at the end. Therefor a mixed function with a square root part and a logarithmic part is tried, where the logarithmic part should make sure that the graph for the torque stays lower. As this approach is still too high at the end a pure logarithmic function was used. The best numerical solution, the mixed function and the logarithmic function are plotted for the height (Fig. 3.8) and the slope of the Cylindrical cam (Fig. 3.9) and the torque of the gear box (Fig. 3.10) over the rotational angle of the Drive shaft. In Fig. 3.10 the relatively good approach of the logarithmic function is shown, especially compared to the other graphs. Remarkable is that the difference between the logarithmic function and the numerical solution is small for the height in the beginning. Although the slope and the torque are derived from the height the difference there is immense. The logarithmic function is

$$s_{log} = 4.87 \cdot ln\left(\frac{(\varphi_s - \varphi_{s,1}) \cdot r_m \cdot s'_{max}}{4{,}87} + 1\right) + s_1 \tag{3.3}$$

which was adjusted to fit the height and the slope of the first section at the beginning. With this function the torque stays always close but below the maximum torque of the gear box. The maximum height for the Cylindrical cam is 9.9 mm (7.3 mm for PT-Mole). Inserting this value in equation (2.19) and with the new compressed length of the Force spring the kinetic energy of the housing is 0.507 Nm. This is an improvement of 67.3 % compared to the PT-design (0.303 Nm).

3.3. Spring rates

Like described in chapter 2 the displacement of the Force and the Brake spring takes place in different phases of the hammering process. Hence the optimal spring rates are not dependent on each other.

3.3.1. Force spring rate

For the Force spring the equations of 2.1 and (2.22) of 2.2 are used. Varying the spring rate doesn't influence the energy transfer model further more. Therefor the optimization is comparable with the spring displacement in 3.2 and influences the displacement as well. The Force spring energy needs to be maximized to gain more output energy of the housing. To avoid worsen effects on the displacement both parameters (displacement s and spring rate c_f) are optimized simultaneous. The spring rate was varied between 0 and 15 N/mm (11.6 N/mm for PT-Mole). For every change in the spring rate the maximum height of the Cylindrical cam is computed which results of an adjusted logarithmic function. This function gives a torque profile similar to the function in 3.2, where the torque is close to the maximum value but always below.

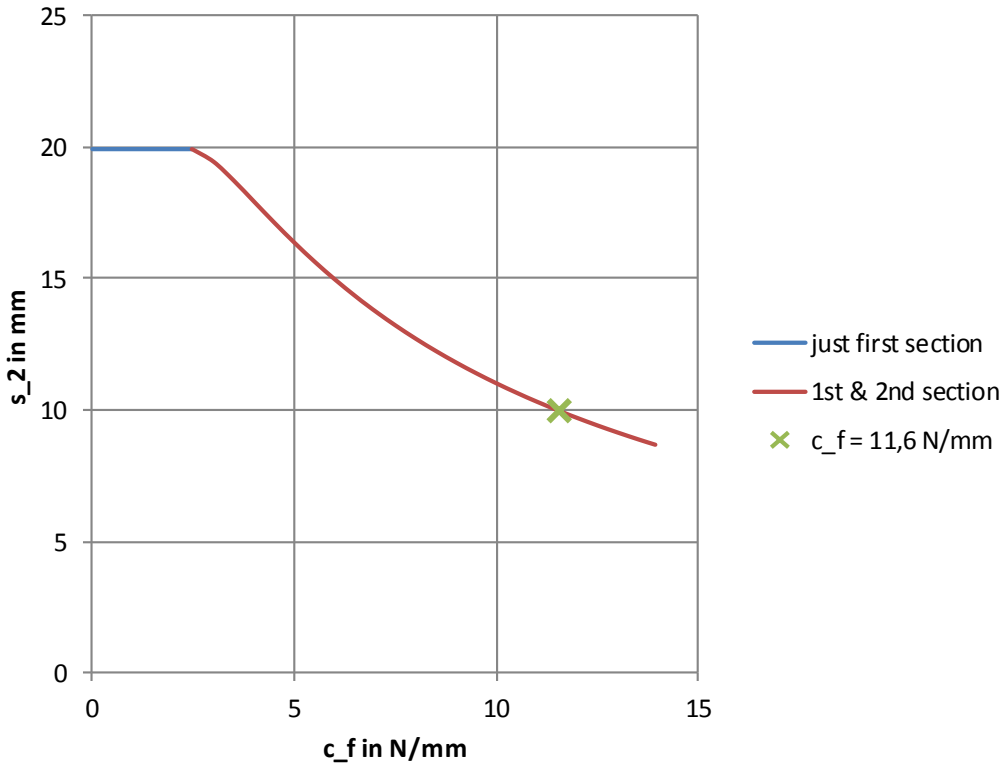

Fig. 3.11: Optimization of Force spring rate – spring displacement

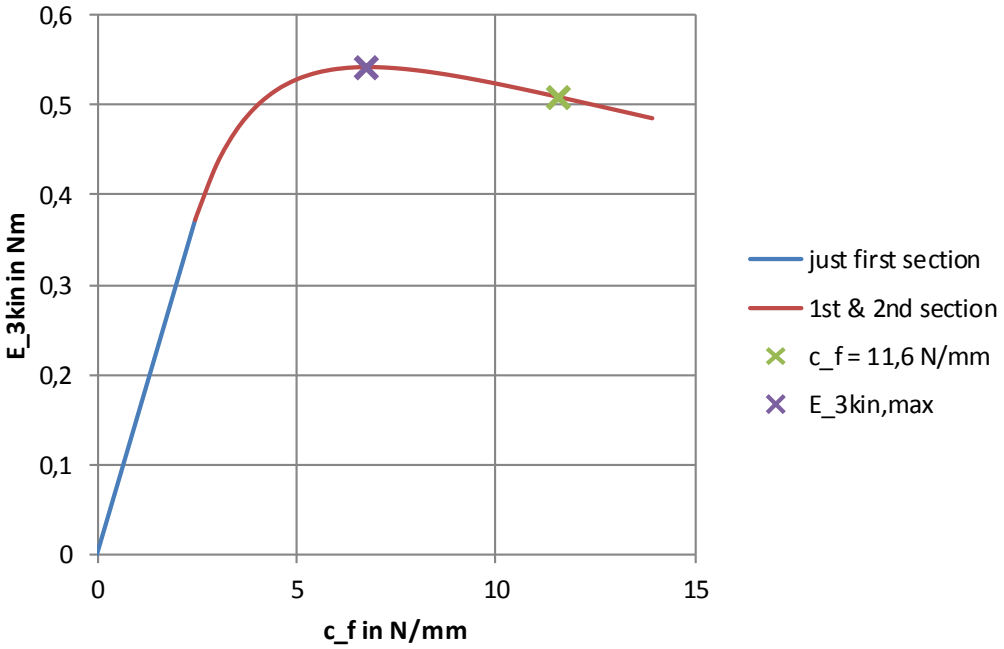

Fig. 3.12: Optimization of Force spring rate – kinetic energy of housing

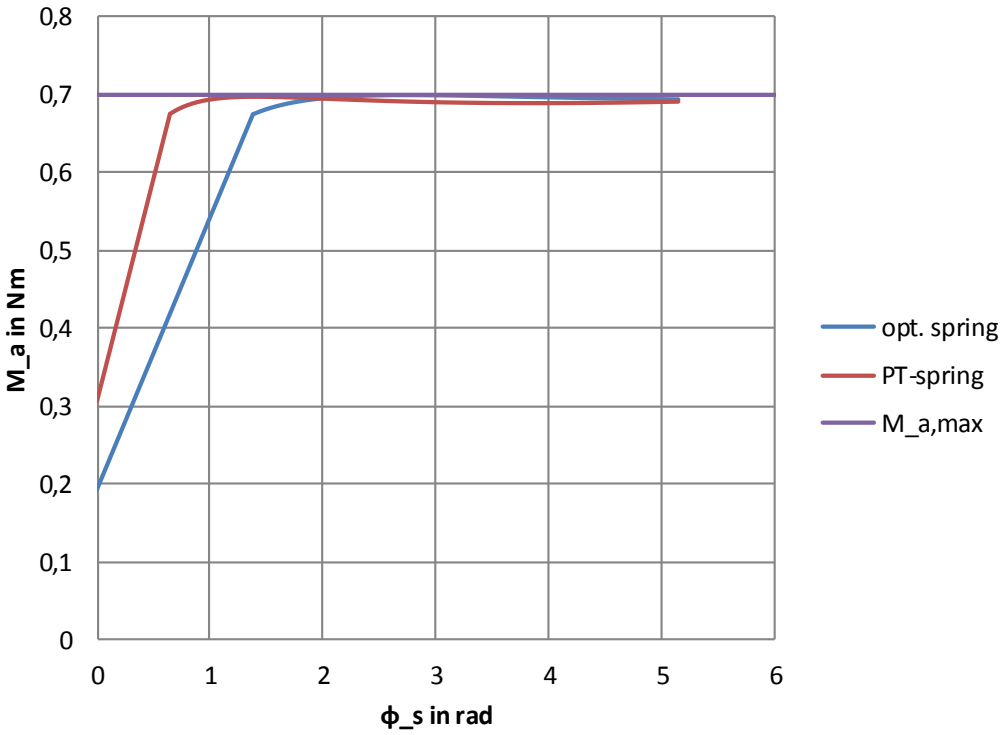

Fig. 3.13: Comparison of optimized Cylindrical cam with PT-spring and with optimized spring

In the figures Fig. 3.11, Fig. 3.12 and Fig. 3.14 the graphs are split in "just first section" and "1st & 2nd section". The theoretical slopes of the Cylindrical cam is partly bigger than the maximum slope defined by the biggest slope of the BB-Mole and PT-Mole design. Where the slope over the complete Cylindrical cam is bigger than the maximum value, the Cylindrical cam contains only of a linear rising ramp (blue part of the graph). In the red part of the graph the linear section at the beginning still exists but also a logarithmic part for the height. Fig.

3.11 shows the realizable spring displacement s_2 with the restrictions of the maximum torque, maximum slope and maximum rotational angle. For the calculated spring displacement with the corresponding Force spring rate the kinetic energy of the housing is displayed in Fig. 3.12. The optimal Force spring rate c_f is at 6.79 N/mm, which enables a kinetic energy of the housing of 0.543 Nm. This results in an improvement of 7.1 % compared to the optimized Cylindrical cam with the PT-spring and 79.2 % compared to the PT-design. In Fig. 3.13 the two torque profiles for the optimized cam with PT-spring and the optimized cam with optimized spring are compared.

The disadvantage of this improvement is an increasing length of the Mole. As the additional height of the Cylindrical cam needs more space inside the hammer the length of the Mole is increasing at least by this value (displayed in Fig. 3.14). This additional space was not needed for the PT-Force spring as there was still enough scope for the increased height of the Cylindrical cam. Furthermore the length of the compressed Force spring needs to be observed so that the parts inside the spring don't interfere. For the maximum kinetic energy of the housing the additional length Δl_{mole} is 4.06 mm.

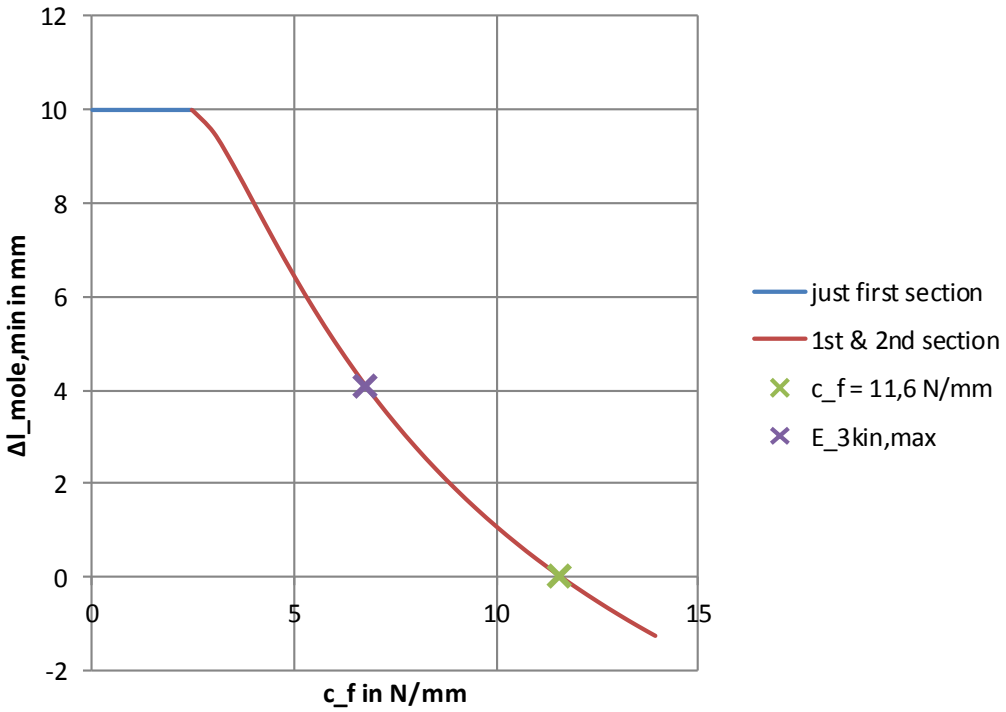

Fig. 3.14: Optimization of Force spring rate – change in overall Mole length

3.3.1. Brake spring rate

The Brake spring rate is a lot easier to investigate. The only influence on the hammering process is its displacement during the movement of the actuator (compare with equation (2.31) in 2.2).

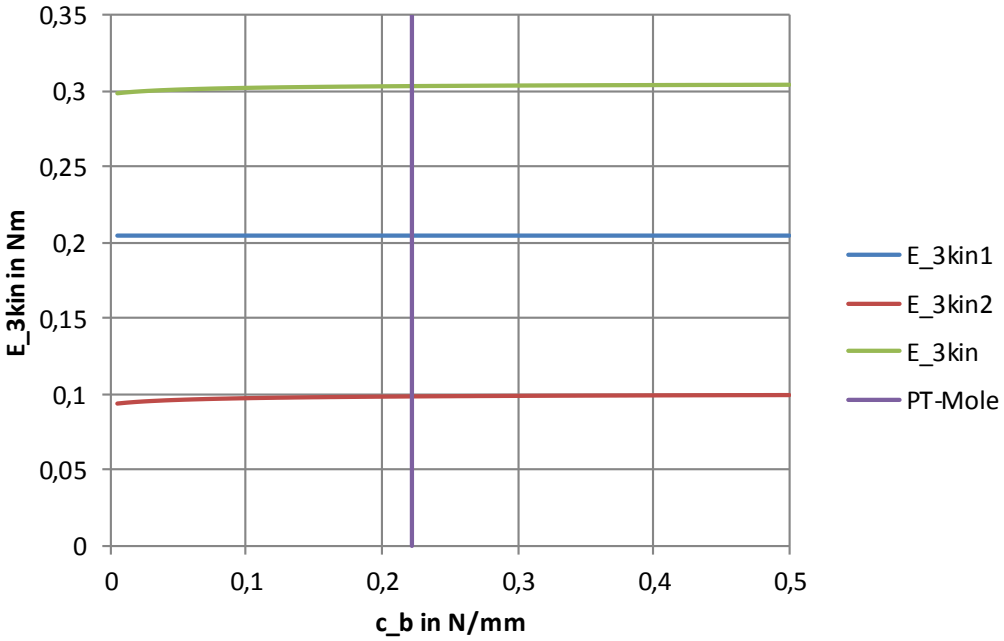

Fig. 3.15: Optimization of the Brake spring rate for the PT-Mole

The spring rate is varied between 0 and 0.5 N/mm. As shown in Fig. 3.15 the influence of the Brake spring rate is only small. The kinetic energy of the housing is rising for a rising Brake spring rate, but the difference between 0.222 N/mm (for the PT-Mole) and 0.5 N/mm is only 0.9 mNm (0.304 Nm total energy) and the improvement is approx. 0.3 %.

3.4. Evaluation

In this passage the changes of the prior investigations are summarized and compared. Furthermore the disadvantages and the effort to realize the improvements are observed and a ranking of priority is created. The enhancements are so far:

Parameter	Improvement to BB-Mole	Improvement to PT-Mole	Disadvantage
mass-ratio PT-Mole	+38.4 %	---	---
optimized mass-ratio (theoretically)	+49.3 %	+7.9 %	not realizable in practice
optimized mass-ratio (with requirements)	+43.4 %	+3.6 %	---
optimized Cylindrical cam	+131.5 %	+67.3 %	---
optimized Force spring rate	+147.9 %	+79.2 %	increased Mole length
optimized Brake spring rate	+38.8 %	+0.3 %	---

Tab. 3.2: Summary of improvements

For realistic mass-ratios the improved Mole-models can be implemented by choosing other dimensions for the relevant parts or choosing materials with other densities. However the unrealistic mass-ratio that used no requirements from the environment is most likely impossible to design, especially when using an equivalent motor as used by the PT-design. Therefor this mass-ratio is disregarded further on. After building the PT-mole the possible enhancement of a new Mole design is low.

The optimized shape of the Cylindrical cam is relatively easy to implement in the CAD-model and with modern CNC-machines also possible to manufacture. Additionally the design of the Mole is only affected at the Cylindrical cam. A first look on the CAD-model suggests that the existing spaces inside the hammer and inside the Force spring are big enough that there is no interference. With a large improvement compared to the already enhanced PT-Mole this change is very advisable to realize.

Using an optimized shape for the Cylindrical cam and change the spring rate of the Force spring at the same time, another small improvement is possible (7.1 % compared to Force spring of the PT-Mole). On the down side, this also includes an increased Mole length and some changes on the parts related to the Force spring to secure enough space for the larger movement of the hammer. The requirements for the length of the Mole due to the available space on the lander, hardly allow any raise of the total Mole length. Therefor the additional length has to be shortened at another part of the Mole. However, this improvement can be considered if other changes are already implemented.

The Brake spring seems to have nearly no influence to the Hammering mechanism. At least for what the mole theory of chapter 2 suggested. Tests with older Mole-versions in the past and first tests with the PT-Mole showed a decreased penetration performance for stiffer Brake springs. The backwards directed movement of the Mole triggered by the actuator movement is not represented well enough in the Mole theory. Therefor the theory has to be reworked with respect to the actuator movement before considering any changes to the Brake spring. So far the Brake spring is kept from the BB- and PT-design.

Ranking

The mass-ratio of the PT-Mole is one of the first realized improvements due to scheduling reasons. For this purpose the housing has to be lighter. As for this model the parts of the housing mass have to be remodeled anyway, the design process takes also places with regard to thin walled parts and lighter materials. The optimized Cylindrical cam is the next to implement since there are only minor changes and a large improvement to the system. A further optimized mass-ratio and the optimized Force spring rate can be considered when remodeling the hammer and actuator in a later process. The Brake spring stays the same so far.

4. Design changes

This chapter explains the modeling of 3D-parts that were designed to fulfill the enhancements of chapter 3. Furthermore the outer shape of the Mole is modified to reduce the resistance force for penetrating the soil.

4.1. Optimized parts of Hammering mechanism

4.1.1. PT-Mole design

At first the Prototype model of the Mole is designed. The mass-ratio that was determined in 3.1.1 is one of the design guidelines. Additionally the outer diameter of the Mole is decreased. A thinner Mole experiences a smaller resistance when penetrating. But as the Hammering mechanism of the PT-Mole stays the same as for the BB-Mole the inner diameter of the housing must be 24 mm. Additionally TEM-A and STATIL has to fit in the new design. The dimensions for the electronics for these systems and the motor are part of the design as well. At the end the assembly of the model has to be regarded, too, so it will be easier as in previous models. This design takes place in close coordination with my supervisor at the DLR, since the design will be used in many tests for the HP³-system to prepare for the InSight mission.

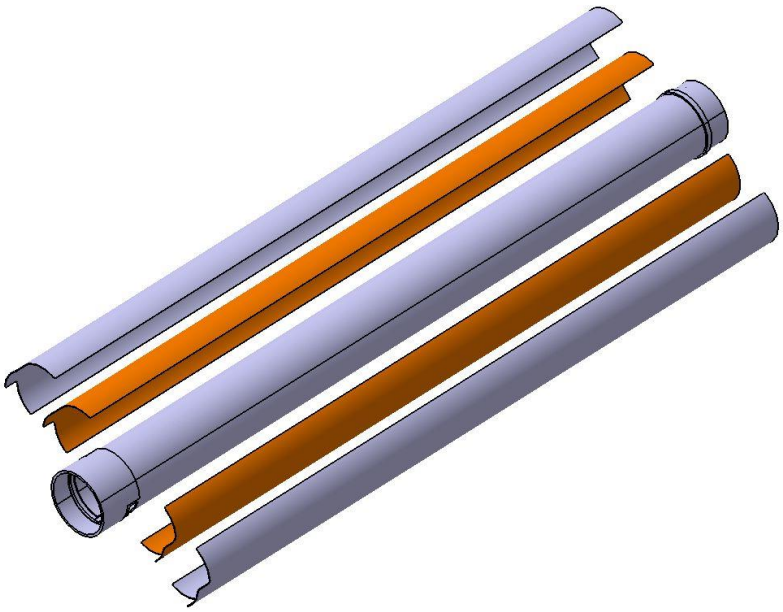

Fig. 4.1: Assembly of TEM-A foils and covers to Outer casing

The main changes compared to the BB-Mole are the removal of the Inner casing that holds the Hammering mechanism and the introduction of a more stable version of the payload

compartment. One of the tasks of the Inner and Outer casings at the BB-Mole is to protect the TEM-A foils against the movement of the Hammering mechanism. The foils were glued on the inner side of the Outer casing, therefor the Outer casing had to be made out of a material with very good thermal conduction. This high strength copper alloy had a relatively high density and thus the housing was heavy, especially with the additional casing on the inside. For the PT-model the Inner casing is removed. To avoid direct contact between TEM-a foils and Hammering mechanism and also to allow an easier gluing of the foils to the Outer casing, the TEM-A foils are positioned on the outside of the Outer casing. To accomplish this, a protection of the foils has to be implemented. On top of the foils another thin layer of aluminum is glued. These covers are overlapping the foils and protect them against scratches of sand or even embedded stones in the soil. In axial direction of the foils the Outer casing has a bigger diameter. Since moving in the axial direction the biggest stress on the foils could come from shearing forces. The bigger diameter of the massive Outer casing (compared to the glue-foil-glue-aluminum-sandwich structure) is taking these loads. As the electronics of the Mole are on the inside the wires for the TEM-A foils have to be guide through holes in the Outer casing. Fig. 4.1 shows the assembly of the TEM-A foils (orange), the TEM-A covers (outer parts) and the Outer casing (central part). The holes inside the Outer casing are displayed in the bottom left corner, within the part with the bigger diameter. The wires of the TEM-A foils are not displayed in this picture.

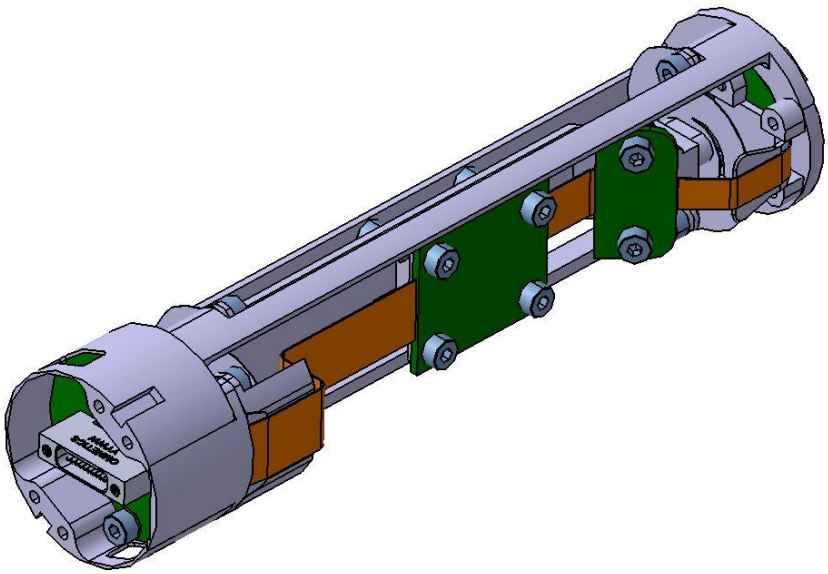

Fig. 4.2: Payload compartment of the PT-Mole

Inside the payload compartment STATIL, the wires to the motor and the interfaces to TEM-A and the Science tether are implemented. STATIL consists of two PCBs mounted on a sled that is damped by two spiral springs (central parts on the inside of the payload compartment in Fig. 4.2). The Payload cage is designed to hold the two springs on both ends of the sled and is therefore made out of one piece. At the top end of the Payload cage (in the front in Fig. 4.2) the Connector PCB is mounted. There are the connectors for TEM-A and the Mole lines of

the Science tether (big connector in the middle of the PCB). Starting from this PCB the wires to STATIL and the motor are guided by a part around the first spiral spring. All these wires go into the first STATIL PCB, then the second STATIL PCB and the motor wires go around the second spiral spring to the Motor PCB at the bottom of the Payload cage. At the second spiral spring another part is guiding the flexprint cable around it. On the Motor PCB the cables to the Motor inside the Brake spring are soldered.

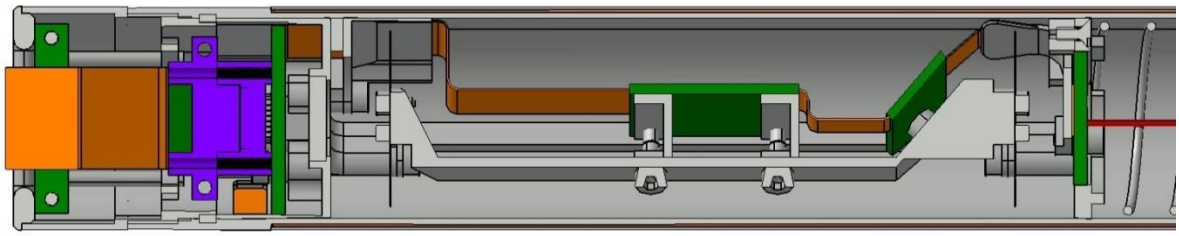

Fig. 4.3: Assembled payload compartment

On top of the Outer casing is the Back casing. It is used to fix the payload compartment to the Outer casing and to hold the cap that closes the Mole (seen on the left side of Fig. 4.3). By introducing this casing it is possible to avoid a bigger outer diameter of the Mole as the fixture points of the payload compartment can be located on a smaller diameter as the inner diameter of the Outer casing. The overall outer diameter of the Mole is 26.4 mm, which is set by the thickness of the sandwich structure of the TEM-A foils and a minimal wall thickness for the Outer casing of 0.5 mm. This light weight design and the fact that the material for all the housing assembly parts is now titanium instead of steel or a copper alloy, decreases the mass of the housing significant. The new housing mass is 0.195 g and the total Mole mass is 0.520 g (compared to the BB-model with 0.552 g housing mass and 0.877 g total mass).

Additionally the sealing concept on the inside of the PT-Mole is more advanced than in the models before. The pot-like shape of the Payload cage is used as an internal seal. All the interfaces between that pot and the surrounding parts are sealed with PTFE-parts. To have a defined path for the air flow during pressure changes (e. g. launching from Earth and landing on Mars) two sintered metal filters are implemented in the cap and in the pot of the Payload cage. They are chosen to be fine enough to avoid soil contamination of the interior through them.

The design of the PT-Mole is undergone several iteration steps. The design of TEM-A and STATIL had to be modified to fit within the PT-Mole. The PT-design also had to change to adjust to the instruments. During this process the PT-Mole is presented to the responsible personal of the different instruments and subsystems. Therefor presentations were made to introduce them to the new design. The presentations were either held by myself or they were held by other colleagues. In Appendix B the designs of the Breadboard-Mole and the Prototype-Mole are compared.

4.1.2. Cylindrical cam design

In section 3.2 the shape of the Cylindrical cam was determined that provides the largest energy output for the housing mass. The shape is also restricted by the maximum values for the torque, the slope and the rotational angle. The logarithmic function, which was an analytical approach to the perfect match for the maximum torque, is transformed in a notation that is suitable for the CAD-program. Enhancing the existing 3D-model for the Cylindrical cam of the PT-design, it is now possible to define the shape of the cam with a function. The rest of this part has stayed the same. The drawing with removed measurements can be found in Appendix C.

4.1.3. Design of other parts

The remaining improvements of chapter 3 or not realized yet. As the project, this thesis is related to, has to focus on only a few changes, only the most promising improvements are tested. However the remaining changes discussed in chapter 3 can be used to investigate the Mole further on after the launch of the mission.

4.2. Design of Tip shapes for testing

In the work of Grygorczuk, et al. [RD 9] and Fish, et al. [RD 7] a different shape for the Tip of the Mole is recommended as the conical tip used by the BB- and PT-Mole. Both groups tested a parabolic shape and compared the penetration performance with several conical shapes (both groups) or a hyperbolic shape (Fish, et al.). The results show that a parabolic shape (or ogive shape) can penetrate approx. 10 to 20 % deeper in the same time. However both works only present one ogive shape that is either not further described [RD 7] or too long for the HP³-Mole (additional 19 mm for the total Mole length) [RD 9].

To find the best ogive for the purpose of the HP³-Mole, several different shapes are investigated. A study with the help of the Mole-simulation won't be successful, since the soil parameters that describe the influence of the tip shape are not known. It wasn't possible to find an extensive study published to this topic so far. There are works of various authors considering the behavior of bullets entering concrete or sand. The topic is indeed very similar to a Mole penetrating soil, but the penetration profile is not close enough to just use this data. Therefor several different ogive shapes are chosen, fit in the requirements for the Tip of the Mole, manufactured and tested (part of 6.3).

4.2.1. Tangent ogive

In [RD 2] the design criteria for a tangent, a secant and a HAACK ogive are described. In Fig. 4.4 the necessary parameters to design a tangent ogive are displayed. To keep the same length as for the conical tip of the PT-design, this length is used for the length L of every

other shape. The radius R for every shape is set by the already existing outer diameter of the PT-Mole. For the tangent tip the ogive radius for the tangent shape ρ_t then calculates to:

$$\rho_t = \frac{R^2 + L^2}{2 \cdot R} \tag{4.1}$$

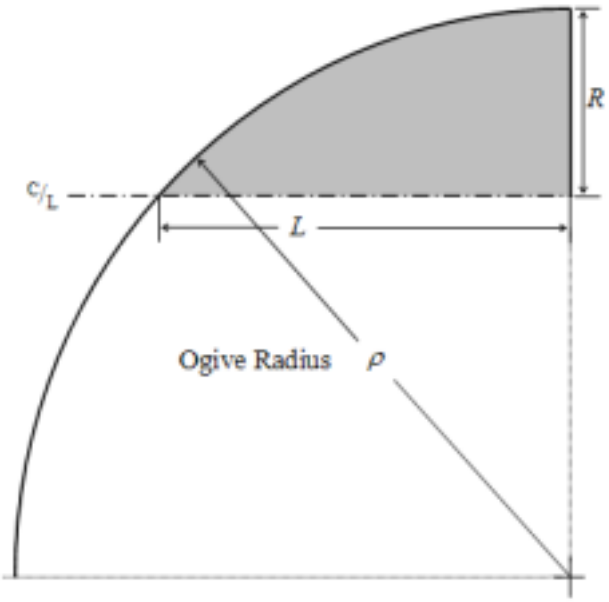

Fig. 4.4: Design criteria for tangent ogive [RD 2]

4.2.2. Secant ogive

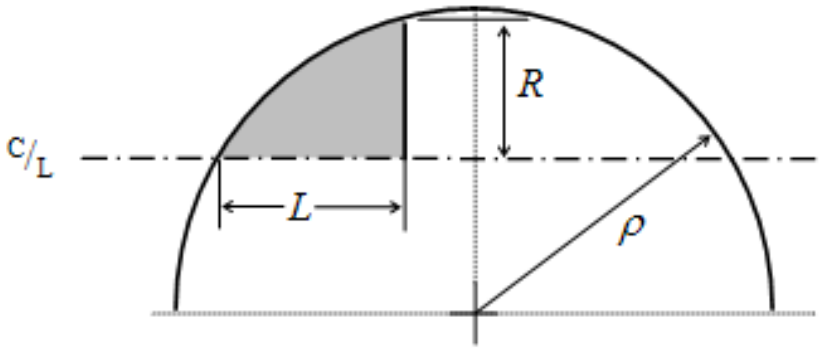

Fig. 4.5: Design criteria for secant ogive [RD 2]

The design parameters for the secant ogive are shown in Fig. 4.5. For this tip the ogive radius for the secant shape ρ_s needs to be set to a value that fulfills the equation:

$$\rho_s > \frac{R^2 + L^2}{2 \cdot R} \tag{4.2}$$

With this radius the secant ogive constant λ is computed by:

$$\lambda = arctan\left(\frac{R}{L}\right) - arccos\left(\frac{\sqrt{R^2 + L^2}}{2 \cdot \rho_s}\right) \tag{4.3}$$

And the radius of the secant ogive r_s is:

$$r_s(h_s) = \sqrt{\rho_s^2 - (\rho_s \cdot \cos\lambda - h_s)^2} + \rho_s \cdot \sin\lambda \tag{4.4}$$

In this equation the height of the secant tip h_s is varying between 0 and L. In this case the ogive radius is set to 35 mm, which results in a clearly different shape compared to the tangent ogive and the cone.

4.2.3. HAACK ogive

The HAACK ogive is not derived from a geometrical figure, but has been analytical determined to be a shape with a minimized drag [RD 11]. The function for the radius of the HAACK ogive r_h is:

$$r_h(\theta) = \frac{R}{\sqrt{\pi}}\sqrt{\theta - \frac{\sin(2 \cdot \theta)}{2} + C_h \cdot \sin^3\theta} \tag{4.5}$$

$$\theta = arccos\left(1 - \frac{2 \cdot h_h}{L}\right) \tag{4.6}$$

With the HAACK ogive variable θ, which is a function of the height of the HAACK ogive h_h (with values from 0 to L). The HAACK ogive constant C_h indicates different types of HAACK ogives. By setting it to C = 1/3 the drag is at the minimum for the given length and volume of the tip. Ogives with a C of 2/3 have a tangent transition to the side walls. In this case the constant was set to 0, which is the minimum drag for given length and diameter of the tip.

4.2.4. Equal pressure ogive

The design criterion for another tip shape is an equal pressure distribution over the tip for every ring segment with the same height. Fig. 4.6 shows a random tip shape which is divided into three ring segments with the same height ($h_1 = h_2 = h_3$). The projected cross-section of each of the three segments should be the same ($A_1 = A_2 = A_3$). With this requirement the pressure is the same for every segment, which should result in a better displacement of the soil.

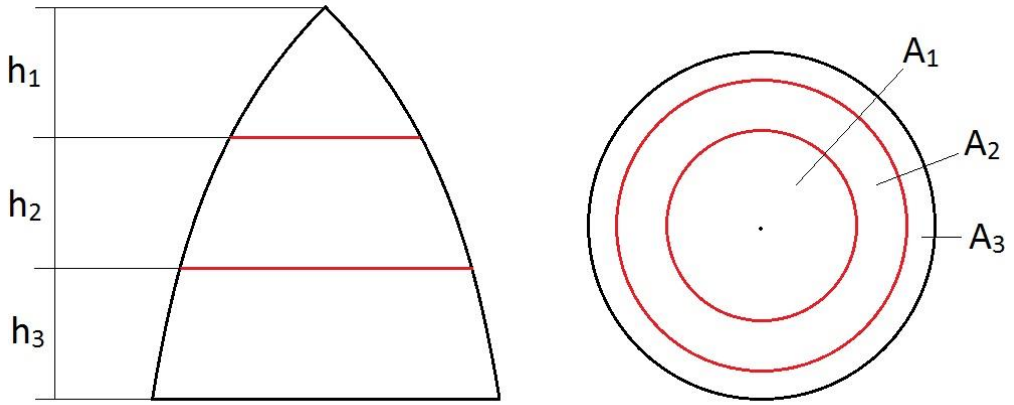

Fig. 4.6: Design criteria of equal pressure tip

Hence the height of the equal pressure ogive h_{ep} at any point must fulfill the equation

$$\frac{h_{ep}}{L} = \frac{\pi \cdot r_{ep}^2}{\pi \cdot R^2} \tag{4.7}$$

so that the amount of the length of the tip L is equal with the amount of the total cross-section. Solved for the radius of the equal pressure ogive r_{ep} (4.7) gives a simple square root function:

$$r_{ep} = R \cdot \sqrt{\frac{h_{ep}}{L}} \tag{4.8}$$

The drawings of the ogive shapes can be found in Appendix D.

4.3. Implementation in CAD-model

4.3.1. PT-Mole design

The assembly of the PT-model parts is already discussed in 4.1.1. As the housing mass was completely new designed the only adaption was made for the Hammering mechanism. Here are the overall length and the diameter the most important values. Additionally the interfaces for the rotational locking at the front and the Brake spring on the back have to be regarded.

4.3.2. Optimized Cylindrical cam

For the optimized Cylindrical cam the changes on the Mole only affects the Cylindrical cam itself. The clearance for the Roller inside the hammer mass and the distance between the parts that extend inside the force spring are big enough that the higher ramp of the Cylindrical cam doesn't cause any problem.

4.3.3. Ogive tips

There are four different tip shapes that need to be tested and compared: the tangent tip, the secant tip, the HAACK tip and the equal pressure tip. The testing will be performed with the PT-Mole. But as in the normal assembly of the PT-Mole the Tip is not easily exchangeable, another solution is needed to allow quick sequenced tests. Therefor the interface between the tip and the Outer casing has changed. An adapter is modeled, that is screwed in the Outer casing instead of the Tip. The adapter stays there for the whole test campaign. The tips however are now fixed to the adapter using four screws. A sealing of this screw connection is not necessary, since the adapter is completely closed towards the Tip. On the other hand the adapter adds additional weight and length to the Mole housing. The results of other tests with the conical tip cannot be used. So a conical tip to fit on the adapter is modeled, too.

To make the tests even more comparable, the masses of all the tips are the same by design. This is adjusted by the way the inside the tip is designed.

Both changes, the optimized Cylindrical cam and the different tips, are designed to be used for the PT-Mole. As a PT-Mole equipped with these parts is not a normal PT-Mole anymore, and this Mole is also not a complete new design, this model is called Hybrid-Mole. Similar to the PT-design the modifications were presented and discussed for several occasions. Both, the PT-Mole and the Hybrid-Mole are tested and compared with each other and the BB-Mole in chapter 6.

5. Stress analysis

In this chapter the stress loads on the parts of the Hammering mechanism and housing assembly are investigated. In [RD 10] an extensive stress analysis is performed. Using the perceptions of this thesis the most critical parts can be determined. They are categorized by their associate assembly and analyzed during this thesis. As two different Mole-models are constructed, the PT-Moe and the Hybrid-Mole are investigated in this chapter.

5.1. Hammer mass

The only likely critical parts of the Hammer mass are the Guide blocks.

Guide blocks

Their purpose is to avoid the rotation of the Hammer inside the Hammer support structure. That is necessary as the rotating Roller inside the Hammer pushes against the Cylindrical cam in axial and tangential direction. Fig. 5.1 shows the parts of the Hammer mass and the location of one Guide block. The second Guide block is located on the opposite position of the first one. The contact pressure between the Guide blocks and the Hammer support structure is the most feasible criterion to validate a sufficient design.

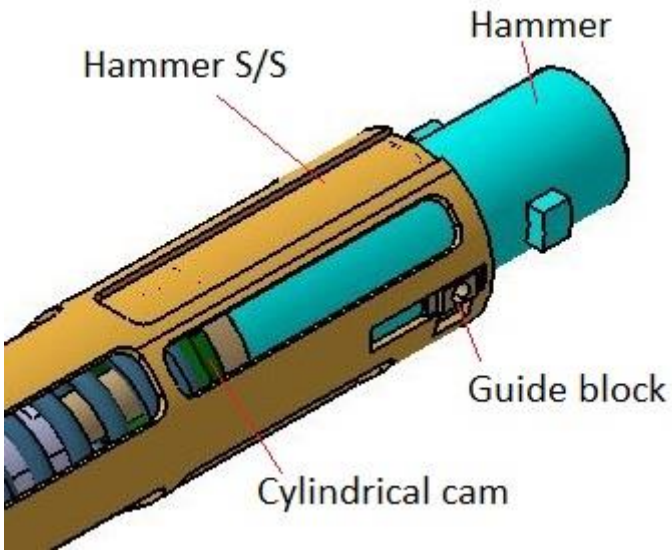

Fig. 5.1: Parts of the Hammer assembly

The contact area is marked in Fig. 5.2. With a few geometrical transformations the contact area between Guide block and Hammer support structure can be computed with:

$$A_{gb} = \left(x_{gb,3} - x_{gb,1}\right) \cdot l_{gb,2} - \left(x_{gb,3} - x_{gb,2}\right) \cdot \left(l_{gb,2} - l_{gb,1}\right) \tag{5.1}$$

The projected lengths $x_{gb,i}$ are given by

$$x_{gb,i} = \sqrt{r_{gb,i}^2 - b_{gb}^2} \tag{5.2}$$

for i = 1; 2; 3. With these equations and the dimensions of the Guide block the contact area can be determined to A_{gb} = 7.36 mm^2.

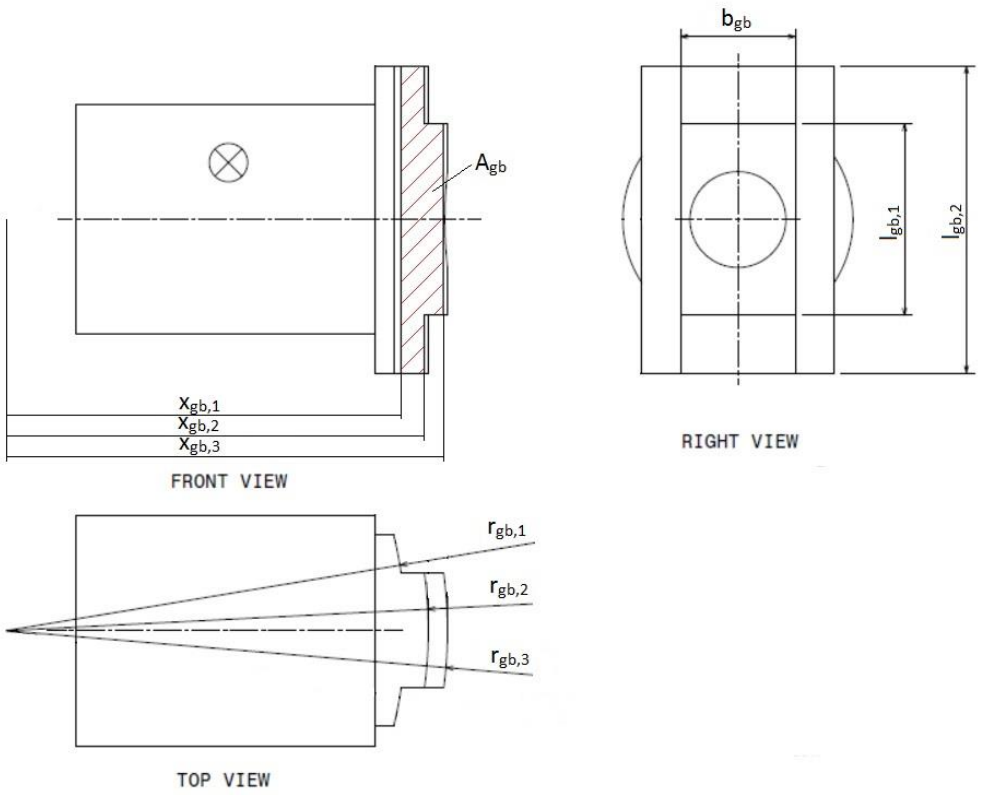

Fig. 5.2: Dimensions of Guide block

The contact pressure p_{gb} can be computed by:

$$p_{gb} = \frac{F_{gb}}{A_{gb}} \tag{5.3}$$

The force on each of the two Guide blocks F_{gb} is stated by the maximum occurring torque $M_{a,max}$ and the mid radius for the contact area $r_{gb,m}$:

$$F_{gb} = \frac{M_{a,max}}{2 \cdot r_{gb,m}} \tag{5.4}$$

Therefor the contact pressure is 4.34 N/mm^2. With an allowed contact pressure $p_{al,\,CA104}$ of 25 N/mm^2 for the copper alloy CA104 the safety factor for the Guide blocks S_{gb} is 5.76 and is valid for the PT-Mole and the Hybrid-Mole.

$$S_{gb} = \frac{p_{al,CA104}}{p_{gb}} \tag{5.5}$$

5.2. Actuator mass

The most critical parts of the Actuator assembly are the Roller , the Roller axle, the Drive shaft and the Extension drive shaft bush. As examples the validation of the Roller and the Extension drive shaft bush are shown in this section.

Roller

The durability approval of the Roller concentrates on the contact pressure between Roller and Cylindrical cam. For this load the shape modification hypothesis is used to calculate the equivalent stress σ_{vg} for the three local coordinates of the Roller:

$$\sigma_{vg} = \frac{1}{\sqrt{2}} \cdot \sqrt{(\sigma_x - \sigma_y)^2 + (\sigma_y - \sigma_z)^2 + (\sigma_z - \sigma_x)^2} \tag{5.6}$$

$$\sigma_x = -2 \cdot \nu \cdot \left(\sqrt{1 + \left(\frac{z}{b}\right)^2} - \frac{z}{b} \right) \cdot p_{r,max} \tag{5.7}$$

$$\sigma_y = -\left(\frac{1 + 2 \cdot \left(\frac{z}{b}\right)^2}{\sqrt{1 + \left(\frac{z}{b}\right)^2}} - 2 \cdot \frac{z}{b} \right) \cdot p_{r,max} \tag{5.8}$$

$$\sigma_z = -\left(\frac{1}{\sqrt{1 + \left(\frac{z}{b}\right)^2}} \right) \cdot p_{r,max} \tag{5.9}$$

with the ratio of depth and contact area width z/b, the POISSON's ratio v and the maximum HERTZian stress $p_{r,max}$. The maximum HERTZian stress occurs at the inner radius of the Cylindrical cam r_i (compare with [RD 10]) and is given by

$$p_{r,max} = \sqrt{\frac{F_{br,max} \cdot E_{X12}}{\cos\alpha \cdot 2\pi \cdot l_r \cdot R_i \cdot (1 - \nu^2)}} \tag{5.10}$$

$$l_r = \frac{R_a - R_i}{\sin\alpha} \tag{5.11}$$

with the maximum occuring load force of the Roller $F_{br,max}$ (determined in 2.1), the YOUNG's modulus of MarvalX12 E_{X12}, the inclination of the Roller path α, the contact length between Roller and Cylindrical cam l_r and the radii of the Roller at the inner (R_i) and the outer (R_a) radius of the Cylindrical cam. The values of the PT-Mole and the Hybrid-Mole are the same except for the maximum occurring load force of the Roller. For the PT-Mole this value is 117.1 N, for the Hybrid-Mole 147.4 N. Hence the maximum HERTZian stress is 757.4 N/mm^2

for the PT-Mole and 849.8 N/mm^2 for the Hybrid-Mole. The maximum values for the equivalent stress are 414.2 N/mm^2 for the PT-Mole and 464.8 N/mm^2 for the Hybrid-Mole.

Therefore the safety factors for these models are 2.66 (PT-Mole) and 2.37 (Hybrid-Mole) with the use of MarvalX12 for the Roller. The equation for the safety factor for the Roller S_r is

$$S_r = \frac{R_{p0.2,X12}}{\sigma_{vg,max}} \tag{5.12}$$

with the yield strength of MarvalX12 $R_{p0.2,X12}$.

Extension drive shaft bush

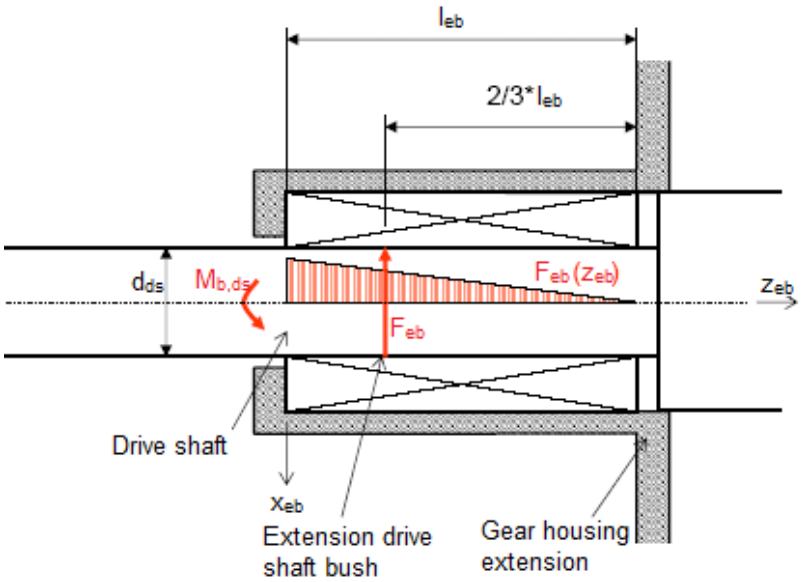

Fig. 5.3: Loads on the Extension drive shaft bush

The Extension drive shaft bush was introduced to carry the bending moment generated by the forces on the Roller. In the worst case only this bush is carrying the loads and the Drive shaft bush is unloaded, if a mismatch in tolerances occurs. To simplify the conditions it is assumed that the bending moment of the Drive shaft $M_{b,ds}$ is affecting the Extension drive shaft bush over the its length l_{eb} and that the progression is linear over the length (compare with Fig. 5.3). The bending moment can then be replaced by a reaction force on the Extension bush F_{eb}. This force steps in at z_{eb} = 1/3 * l_{eb}.

$$M_{b,ds} = F_f * r_m \tag{5.13}$$

$$F_{eb} = \frac{3 \cdot M_{b,ds}}{2 \cdot l_{eb}} \tag{5.14}$$

with the Force spring force F_f steps in with the lever arm r_m, which is the mid radius of the Cylindrical cam. The bending moment is 642.5 mNm for the PT-Mole and 820.1 mNm for the

Hybrid-Mole. Therefor are the values for the reaction force on the Extension drive shaft bush 321.3 N at the PT-model and 410.1 N at the Hybrid-model.

The criterion for the mechanical stress is the reaction force carried by the projected bush area:

$$p_{eb} = \frac{F_{eb}}{l_{eb} \cdot d_{ds}} \tag{5.15}$$

This specific bush load p_{eb} is 17.9 N/mm^2 for the PT-Mole and 22.8 N/mm^2 for the Hybrid-Mole. With the allowed contact pressure $p_{al,CA104}$ for CA104, the material of the Extension drive shaft bush, of 25 N/mm^2 the safety factor S_{eb} is determined to:

$$S_{eb} = \frac{p_{al,CA104}}{p_{eb}} \tag{5.16}$$

The PT-Mole has a safety factor of 1.40 and the Hybrid-Mole a safety factor of 1.10. These values are very low, but still above 1. However the worst case of only one loaded bush on the Drive shaft should be avoided by choosing appropriate tolerances for the bushes.

5.3. Housing mass

The only critical part of the housing mass is the Tip as the strokes of the Hammering mechanism hit it on the inside.

Tip

For the Tip the fatigue stress due to the strokes is investigated. To regard the worst case, it is assumed that the complete energy difference of the Hammer before ($E_{1,kin}$) and after the first stroke ($E_{1,kin,p}$) is transformed in potential energy of the housing $U_{pot,ho}$. Therefor the Outer casing would deform.

$$U_{pot,ho} = E_{1,kin} - E_{1,kin,p} = \frac{1}{2} \cdot c_{oc} \cdot x_{oc}^2 \tag{5.17}$$

with the spring rate of the Outer casing c_{oc} and the deformation of the Outer casing x_{oc}. This could be realized by fixing the end of the Outer casing. The housing wouldn't move after the stroke and the additional energy would be used to deform the thin walled Outer casing. The deformation is determined by (5.13):

$$x_{oc} = \sqrt{\frac{2 \cdot \left(E_{1,kin} - E_{1,kin,p}\right)}{c_{oc}}} \tag{5.18}$$

The spring rate of the Outer casing is calculated by:

$$c_{oc} = \frac{E_{Ti} \cdot \pi \cdot \left(D^2 - d_{i,oc}^2\right)}{4 \cdot l_{oc}} \tag{5.19}$$

with the YOUNG's modulus E_{Ti} of TiAl6V4, which is the material of the Outer casing, the outer diameter of the Mole D, which is also the outer diameter of the Outer casing, the inner diameter of the Outer casing $d_{i,oc}$ and the length of the Outer casing l_{oc}. This equation is a simplification, as in reality the Outer casing is covered with the sandwich structure of TEM-A, glue and the covers. For the PT-Mole and the Hybrid-Mole the spring rate is 36200 N/mm. Using the derivation of the kinetic energy of the hammer before and after the first stroke in 2.2, the deformation of the Outer casing is then calculated to 0.133 mm for the PT-Mole and 0.172 mm for the Hybrid-Mole.

With the deformation and the spring rate of the Outer casing, the stroke force for the first stroke F_{stroke} is determined by:

$$F_{stroke} = c_{oc} \cdot x_{oc} \tag{5.20}$$

For the PT-Mole this force is 4810 N, for the Hybrid-Mole it is 6230 N. As the energy of the second stroke is smaller as the first stroke, the biggest loads occur for the first stroke. The compressive stress on the Tip σ_t is defined by the stroke force effect on the contact area of the Hammer and the Tip A_{stroke}.

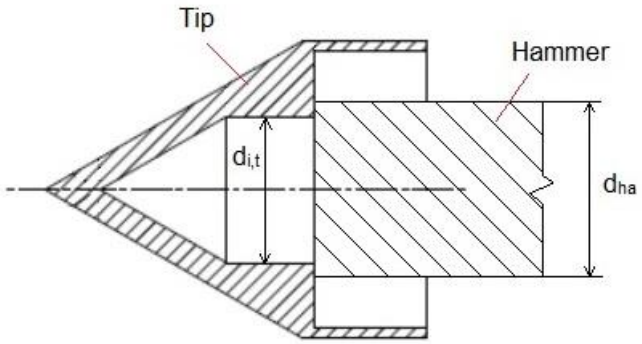

Fig. 5.4: Contact area of Hammer and Tip

$$\sigma_t = \frac{F_{stroke}}{A_{stroke}} \tag{5.21}$$

$$A_{stroke} = \frac{\pi}{4} \cdot \left(d_{ha}^2 - d_{i,t}^2\right) \tag{5.22}$$

Where the diameter of the Hammer d_{ha} and the inner diameter of the Tip $d_{i,t}$ are used to calculate this contact are. For both investigated Mole-models the contact area is 68.3 mm^2. The compressive stress of the Tip is 70.4 N/mm^2 for the PT-Mole and 91.2 N/mm^2 for the Hybrid-Mole.

The safety factor for the Tip S_t is determined by the allowed fatigue stress for TiAl6V4 $\sigma_{fa,Ti}$, the material of the Tip:

$$S_t = \frac{\sigma_{fa,Ti}}{\sigma_t} \tag{5.23}$$

With the value for the allowed fatigue stress of 580 N/mm^2 the safety factor of the PT-Mole is 8.24 and of the Hybrid-Mole 6.36.

Additional to the mentioned critical parts the safety factors of several other parts are calculated roughly. All safety factors are big enough to be sure that no part is damaged during operations of the Mole.

6. Verification of improvements

This chapter treats the validation of the theoretically determined improvements with test data. The most obvious way to test the different Mole-models is to perform penetration tests in the same soil and with the same conditions. However, there are several disadvantages for these tests. The duration of one single test is very long. Before each test the soil needs to be prepared in the same way. Hence the soil needs to be freshly filled into the testbed. Even then it is uncertain if the soil is completely comparable with the other tests. To validate this, a penetrometer test needs to take place after each test. During this test several soil parameters can be measured. These parameters help to classify the soil and allow comparisons between different tests. To avoid the complete procedure of a penetration test for the validation of the improvements of this thesis, a test stand is designed.

6.1. Design of Test stand

Several requirements influence the design of a test stand for the Mole. It has to work in controlled conditions so that a calibration of the Test stand is not necessary for every test. The results of the measurement should give some indication for the performance it would have in a soil test bed. The Test stand should use a simple principle to measure the output of the Mole. In the best case the measurements can be easily converted into the desired dimension. The Mole must return to its resting position after each hammering cycle. Hence the Test stand can be used for several cycles and even for long duration tests.

For the measuring principle the deflection of a spring is used. With a spring the kinetic energy of the housing is directly converted into a displacement of the spring. The spring will then return to the precompressed length due to the weight of the Mole. To measure the displacement a distance is used. With a high sample rate the first and the second stroke can be detected separately. This helps to verify the Mole theory as well. Therefor the Test stand needs to position the spring and the Mole in a defined way. The Mole should move freely along its axial direction and the distance sensor needs to be implemented in a sensible way. To realize this a reflection surface for the LASER-sensor needs to be attached on top of the spring.

Fig. 6.1 shows the realized Test stand with a PT-Mole (the Science tether is not attached in this picture). The Mole is positioned on a part that is the negative shape of the cone tip. This part is screwed to a fixture for the measurement spring with the reflection surface in between (squared sheet metal below the triangular plate in Fig. 6.1). The Mole is guided in

axial direction by a pipe mounted on the stand plate (triangular plate in picture). At both ends PTFE-rings are screwed to the pipe that works as sliding bushes for the Mole. The distance sensor is mounted on top of the stand plate and is pointing downwards through a hole in the stand plate on the reflection surface.

Fig. 6.1: Test stand with PT-Mole

The output of the sensor is a voltage that can be converted in a length. The displacement of the stand spring s_s can be determined by building the difference of the measured length to the resting position. With the length of the stand spring in the uncompressed state ($l_{s,u}$) and precompressed state ($l_{s,p}$) the spring energy of the maximum compressed stand spring E_s can be computed:

$$l_{s,c} = l_{s,p} - s_s \tag{6.1}$$

$$E_s = \frac{1}{2} \cdot c_s \cdot \left(\left(l_{s,u} - l_{s,c} \right)^2 - \left(l_{s,u} - l_{s,p} \right)^2 \right) \tag{6.2}$$

Where $l_{s,c}$ is the length of the compressed stand spring and c_s is the spring rate of the stand spring. As seen in Fig. 6.3 the two strokes of one cycle can be read out separately. The total kinetic energy of the housing $E_{3,kin}$ can then be determined by:

$$E_{3,kin} = E_{3,kin,1} + E_{3,kin,2} = E_{s,1} + E_{s,2} + E_{s,fric} \tag{6.3}$$

$$E_{3,kin} = \frac{1}{2} \cdot c_s \cdot \left(\left(l_{s,u} - l_{s,c,1}\right)^2 - \left(l_{s,u} - l_{s,p,1}\right)^2 + \left(l_{s,u} - l_{s,c,2}\right)^2 - \left(l_{s,u} - l_{s,p,2}\right)^2 \right) + E_{s,fric} \quad (6.4)$$

Where the indices 1 and 2 stand for the first resp. second stroke. The energy loss by friction $E_{s,fric}$ is induced by friction of the Mole to the PTFE-rings as well as friction inside the stand spring. The portion of this energy of the total kinetic energy of the housing needs to be determined by a calibration. It is dependent on the spring displacement and the Mole which is used in the Test stand.

6.2. *Performance of PT-Mole vs. BB-Mole*

First tests performed with the BB-Mole showed a spring displacement of 1.8 mm for the first stroke in the average of 20 stroke cycles. The second stroke showed a displacement of approx. 0.25 mm. Fig. 6.2 shows a complete test in the Test stand for the BB-Mole. In Fig. 6.3 the diagram is focused on two stroke cycles. The first stroke generates a big spring displacement, the stand spring unloads immediately and the second stroke takes place when the spring passes the resting position for the first time. After that the spring is oscillating until it comes to a rest. The difference between the local maxima and minima in this phase can be used to determine the friction losses in the Test stand. There is no additional energy transferred by the Mole to the stand spring in this phase.

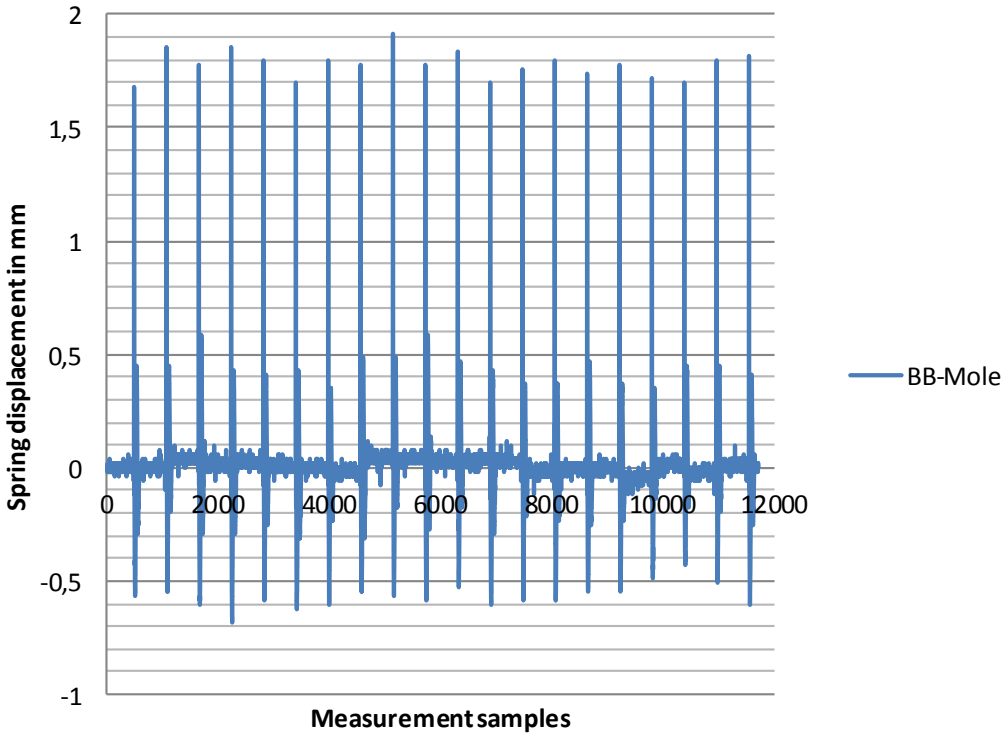

Fig. 6.2: Complete performance test of the BB-Mole

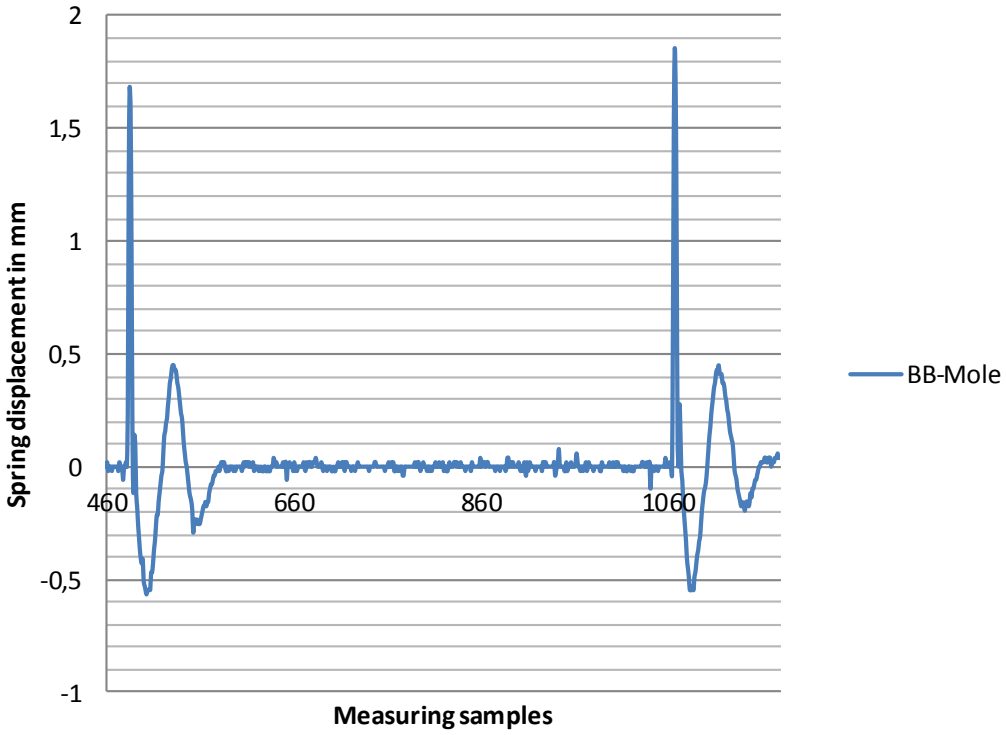

Fig. 6.3: Scope on the strokes of two cycles for the BB-Mole

The performance tests of the PT-Mole show similar graphs but with an average spring displacement for the first stroke of 5.4 mm. The second stroke can hardly be seen as the sample rate was decreased immensely. The reason for that couldn't be figured out during this thesis. The Test stand calibration has not finished until the end of this thesis, so a complete comparison of the BB-Mole to the PT-Mole is not possible. However, the spring energy of the stand spring is determined to 0.0125 Nm for the first stroke of the BB-Mole and 0.045 Nm for the first stroke of the PT-Mole. These values suggest an increase of 260 % in the performance of the PT-Mole. But as described above, additional information is needed to get a good comparison of the two Moles. If the energy losses don't rise linearly with the kinetic energy of the housing, the increase could be lower or higher.

Remarkable is the fact, that the stand spring energy is significant lower than the expected kinetic energies of the housing (e. g. 0.309 Nm for the PT-Mole). This is also seen in the small deflection of the stand spring. The spring was selected to perform a deflection of half of the sensor range of 40 mm for the PT-Mole. Either the energy losses of the Test stand take most of the energy of the housing or the Mole theory outputs too high values for this energy. It is also possible that the measurement method is not suitable for the shock loads. If the stand spring is not behaving like expected, the results can be wrong as well. This topic needs to be investigated further in a future work.

6.3. Performance of Hybrid-Mole vs. PT-Mole and BB-Mole

During this thesis the optimized Cylindrical cam and the different tips were manufactured. But the PT-design showed some problems that needed to be solved prior to realize the

Hybrid-Mole. Therefor a test campaign with the Hybrid-Mole couldn’t proceed in this thesis. The assembly and tests of the Hybrid-Mole need to take place in a future work.

Furthermore is the Test stand only able to detect the kinetic energy of the housing mass. The improvements with the smaller outer diameter and the tip shapes cannot be tested. For these parts penetration tests in soil are needed. These tests will be performed in the future as well.

7. Conclusion

In this thesis the Mole theory is investigated with respect to potential improvements. To implement a more complex shape for the Cylindrical cam the way its parameters affect the system is enhanced. Instead of constant slopes, it is now possible to use a function for the shape. After the changeable parameters, that affect the energy output of the Mole, are summarized in the expression

$$E_{3,kin} = f(c_b, c_f, m_1, m_2, m_3, s_2) \tag{7.1}$$

each of these parameters is analyzed.

The mass ratio was optimized in a first step to fit the restrictions for the PT-Mole design. Therefore the masses m_1 and m_2 don't change, but the mass m_3 is varied. The optimal housing mass for this case is determined and is used as a design criterion of the PT-Mole. The masses are then considered as free variables to look for the optimal mass-ratio. After introducing reasonable restrictions for the masses, a realizable mass-ratio is computed. To enhance the Force spring displacement it has to rise to its maximum possible value for the given requirements. Therefor the shape of the Cylindrical cam was changed to use the maximum gear box torque for a longer period. A change of the Force spring rate affects this shape and also the length of the Mole. Hence the analysis suggests a smaller spring rate, which needs more space inside the Hammering mechanism. Changing the Brake spring shows nearly no effect on the Mole performance, at least with this Mole theory. All these changes are evaluated by their gain for the performance, the effort of implementing them and the disadvantages they introduce to the Mole.

The most efficient improvements are realized, first as a CAD-model. The biggest potential of the change in the mass-ratio is realized in the PT-Mole-design, which is part of this thesis. Hence a complete redesign of the housing mass is performed. During this design the instruments and electronics of the HP³-Mole are integrated as well. For the Cylindrical cam the 3D-model is issued, too. With regard to the work of other institutions the usage of another tip is considered, which should decrease the penetration resistance of the soil. As this cannot be implemented in the soil-model, several different ogive shaped tips are designed. To test these tips without disassembling the Mole, an adapter was designed as well, where the tips can be easily screwed to.

The designs of the PT-Mole and the Hybrid-Mole are then examined with respect to the stress levels of critical parts. The change of material and higher loads are introduced by the improvements. After the confirmation of the safety margins for the parts, they were manufactured.

In the Test stand, which is designed during the work of chapter 6, the different Mole-models can be compared with respect to the kinetic energy of the housing. The calibration of the Test stand is not yet matured. Hence only a rough comparison of the BB-Mole and the PT-Mole was possible. There it was possible to show a significant improvement, but the exact value for that needs the energy losses inside the Test stand as well. The Hybrid-Mole was not assembled so far. Therefor the comparison of this model to the previous ones is not possible yet.

7.1. Future work

During the progression of this thesis the Mole theory at the current state showed some inadequateness. The theory needs a closer look for the role of the Brake spring and the friction losses inside the Hammering mechanism. The measured energy output at the stand spring is smaller by more than a magnitude. At this point it is also possible that the friction losses inside the Test stand are too big. A calibration of the Test stand for every Mole-model is necessary.

The test campaign for validating the tip shapes needs to take place. Representative results are not only useful for choosing the best option for the HP³-Mole. But some correlations between the tip shapes and their soil parameters will improve the comprehension of the Mole-soil-interaction.

For future work, most likely after the InSight mission has launched, the other mentioned changes should be considered as well. Therefor the performance of the Mole can be enhanced further and the selection of a Mole for future missions is likelier.

List of literature

[RD 1] **Beitz, W., Grote, K.-H.**, *Dubbel Taschenbuch für den Maschinenbau*, Springer-Verlag, Berlin, 19. edition, 1997

[RD 2] **Crowell, G. A.**, *The Descriptive Geometry of Nose* Cones, http://de.scribd.com/doc/60921375/The-Descriptive-Geometry-of-Nose-Cone, last checked : 15.09.2013

[RD 3] **DLR**, *Heat Flow and Physical Properties Package*, http://www.dlr.de/pf/desktopdefault.aspx/tabid-8653, last checked: 10.09.2013

[RD 4] **DLR**, *Rosetta*, http://www.dlr.de/rb/de/desktopdefault.aspx/tabid-4538/7439_read-11269/, last checked: 10.09.2013

[RD 5] **Faulhaber**, *Technical Data for products*, http://www.faulhaber.com/, last checked: 19.08.2013

[RD 6] **Fischer, U., et al.**, *Tabellenbuch Metall*, Verlag Europa-Lehrmittel, Haan-Gruiten, 42. edition, 2002

[RD 7] **Fish, C. S., Ban, H., Sellers, S., White, J., Wouden, A., Allen, D.**, *Heat Flow Probe for Lunar and Planetary Missions*, American Geophysical Union, Fall Meeting 2009

[RD 8] **Große, J.**, *Simulation and parameter studies for the conceptual design of a combined thermal and mechanical penetration mechanism for icy planetary bodies*, Diploma thesis Universität Bremen, 2010

[RD 9] **Grygorczuk, J., Seweryn, K., Wawrzaszek, R., Banaszkiewicz, M.**, *Technological Features in the New Mole Penetrator "KRET"*, 13th European Space Mechanism and Tribology Symposium, Wien, 2009

[RD 10] **Grzesik, A.**, *Konstruktion eines Schlagmechanismus für einen instrumentierten Penetrator zur Bodenerkundung bei Planetenmissionen (Mercury Surface Element)*, Diploma thesis Fachhochschule Aachen, 2004

[RD 11] **Haack, W.**, *Geschoßformen kleinsten Wellenwiderstandes*, Bericht 139 der Lilienthal-Gesellschaft, 1941

[RD 12] **Historic Spacecraft**, *Discovery Program Missions*, http://historicspacecraft.com/Probes_Discovery.html, last checked: 10.09.2013

[RD 13] **NASA**, *Discovery Program*, http://discovery.nasa.gov/index.cfml, last checked: 19.08.2013

[RD 14] **NASA**, *Goddard Space Flight Center*, http://www.nasa.gov/centers/goddard/news/releases/2011/11-033.html, last checked: 20.08.2013

[RD 15] **NASA**, *InSight*, http://insight.jpl.nasa.gov/home.cfm, last checked: 10.09.2013

[RD 16] **Spohn, T., et al.**, *InSight: Measuring the Martian heat flow using the Heat flow and Physical Properties Package (HP³)*, 43rd Lunar and Planetary Science Conference, The Woodlands, 2012

[RD 17] **Stoker, C. R., Gonzales, A., Zavaleta, J. R.**, *Moon/Mars Underground Mole*, http://esto.nasa.gov/conferences/nstc2007/papers/Gonzales_Andy_C10P1_NSTC-07-0117.pdf, Download: 10.09.2013

Appendix A Simulation output

The output of the Mole-simulation contains graphs for the rotation speed of the motor, the motor current, the rotation speed of the gear box, the power consumption and the gear box torque over rotational angle. Furthermore the penetration depth over the designated simulation time is given.

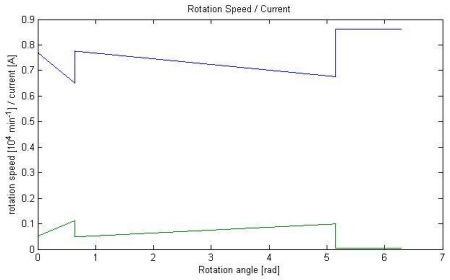

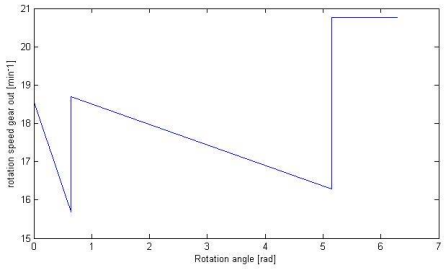

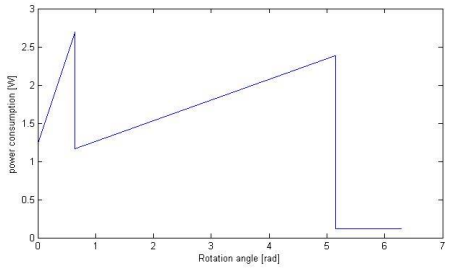

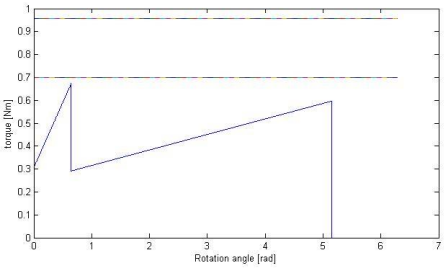

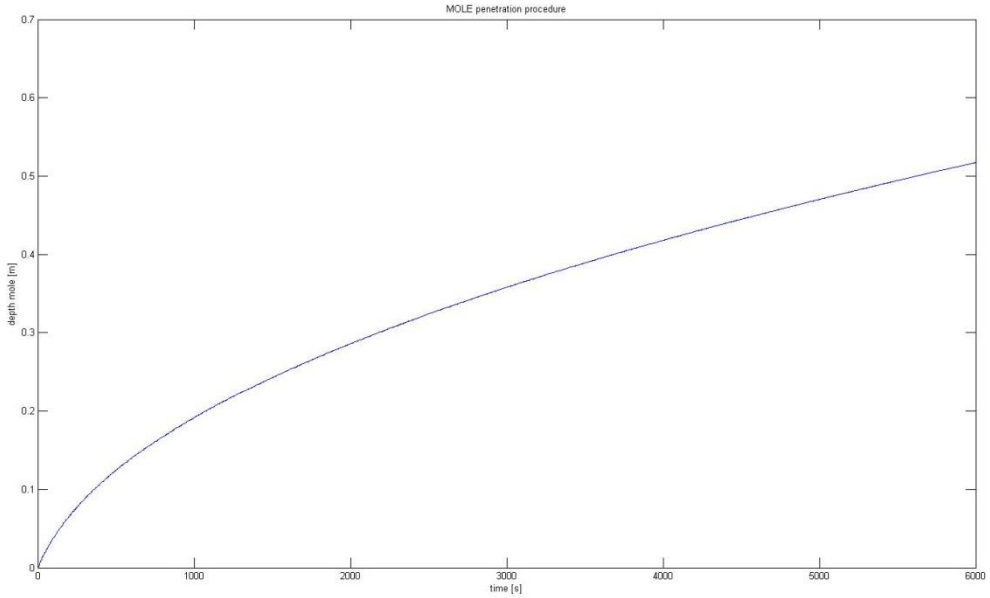

Appendix B Comparison BB-Mole and PT-Mole

In the pictures below a comparison of the PT-Mole (left) and the BB-Mole (right) is shown. The hammer mass (green), actuator mass (turquoise) and housing mass (orange) are highlighted.

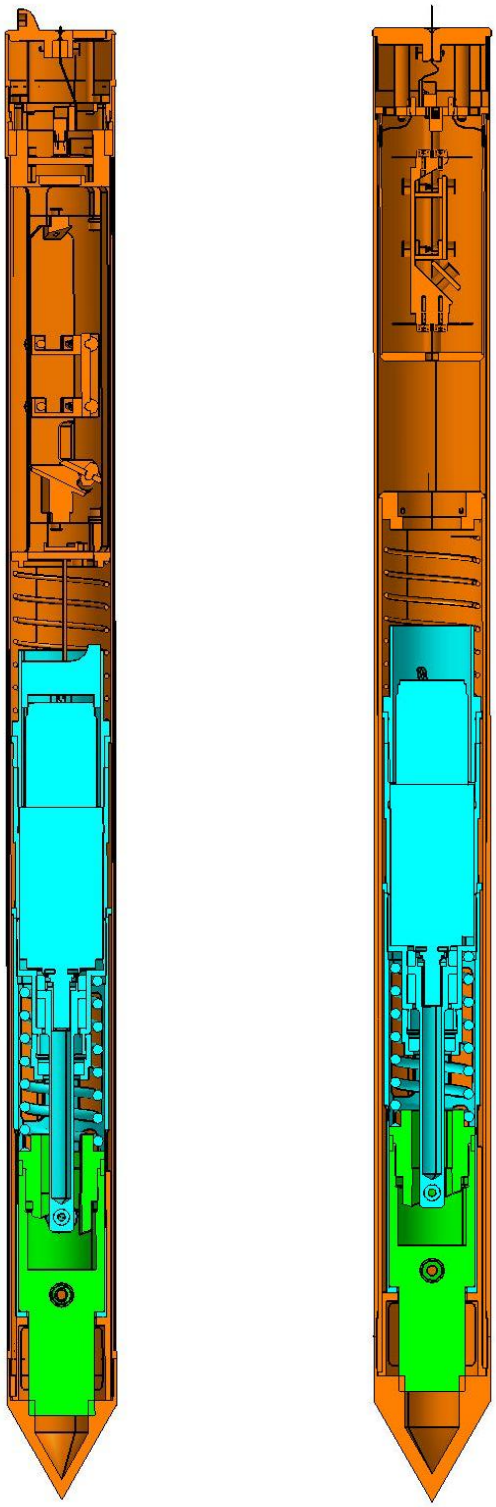

Appendix C Drawing of optimized Cylindrical cam

Drawing of the optimized Cylindrical cam for the PT-model Force spring. Measurements are removed.

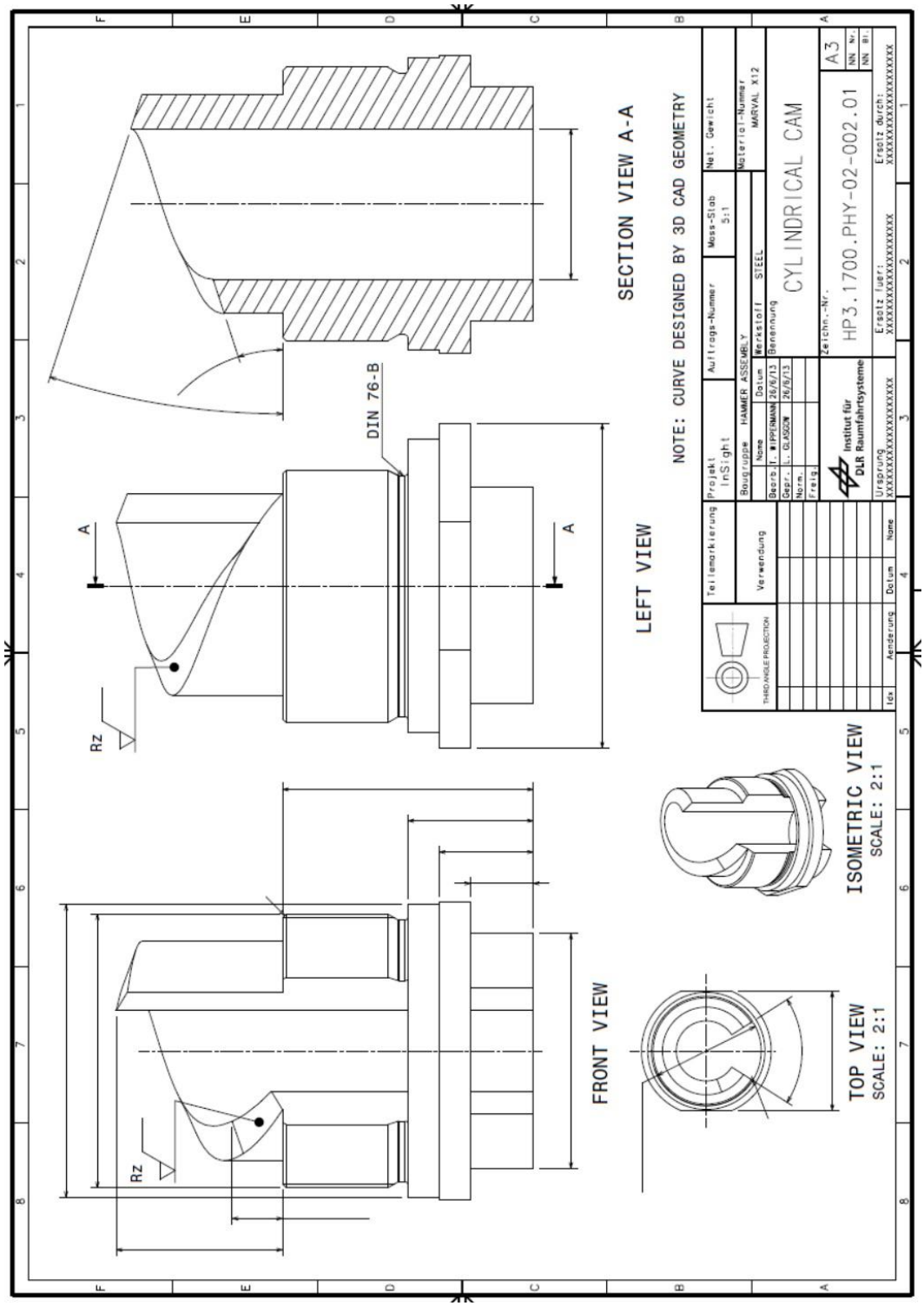

Appendix D Drawings of different tips and Tip adapter

Drawing of the conical tip with removed measurements:

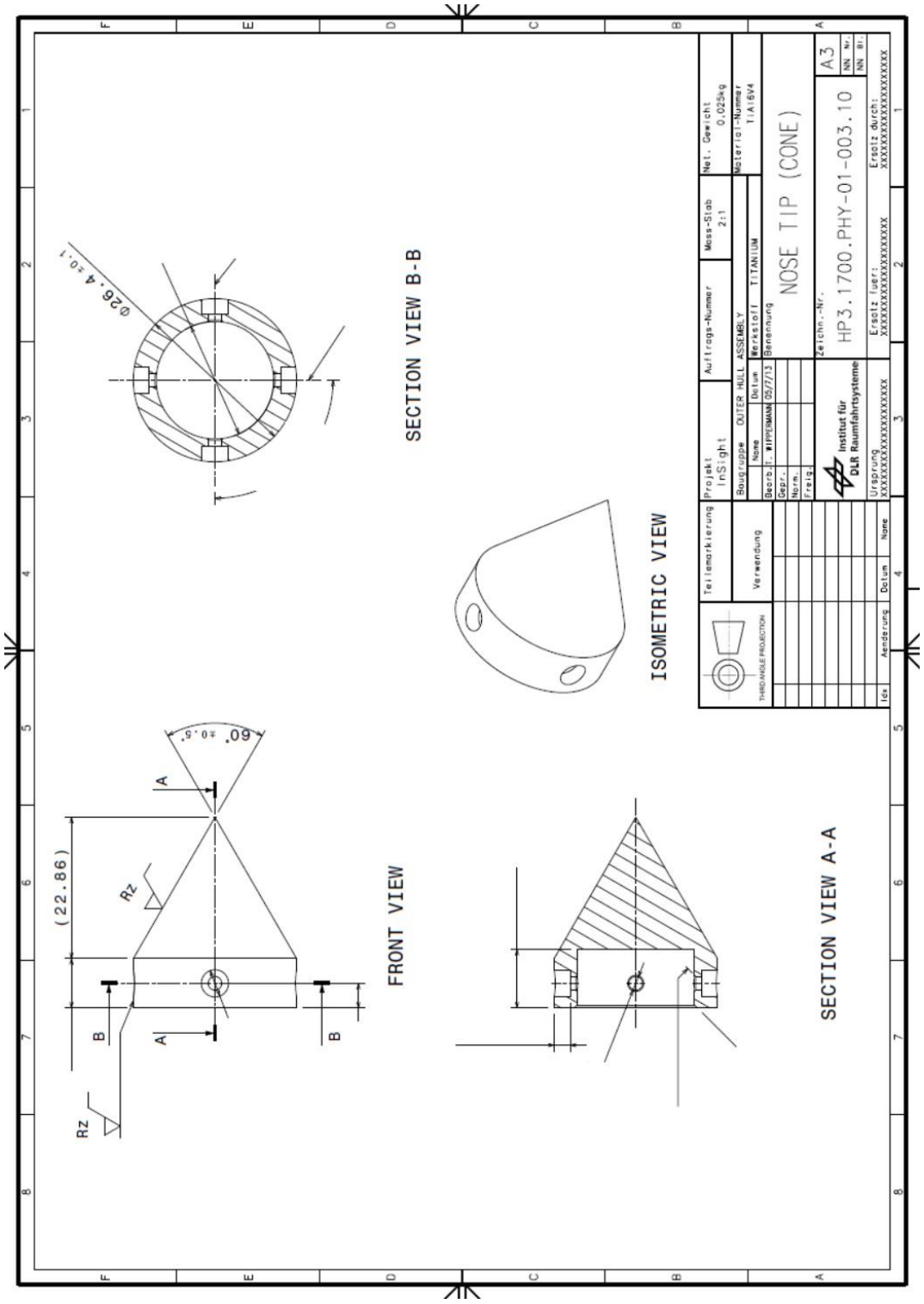

Drawing of the tangent tip with removed measurements:

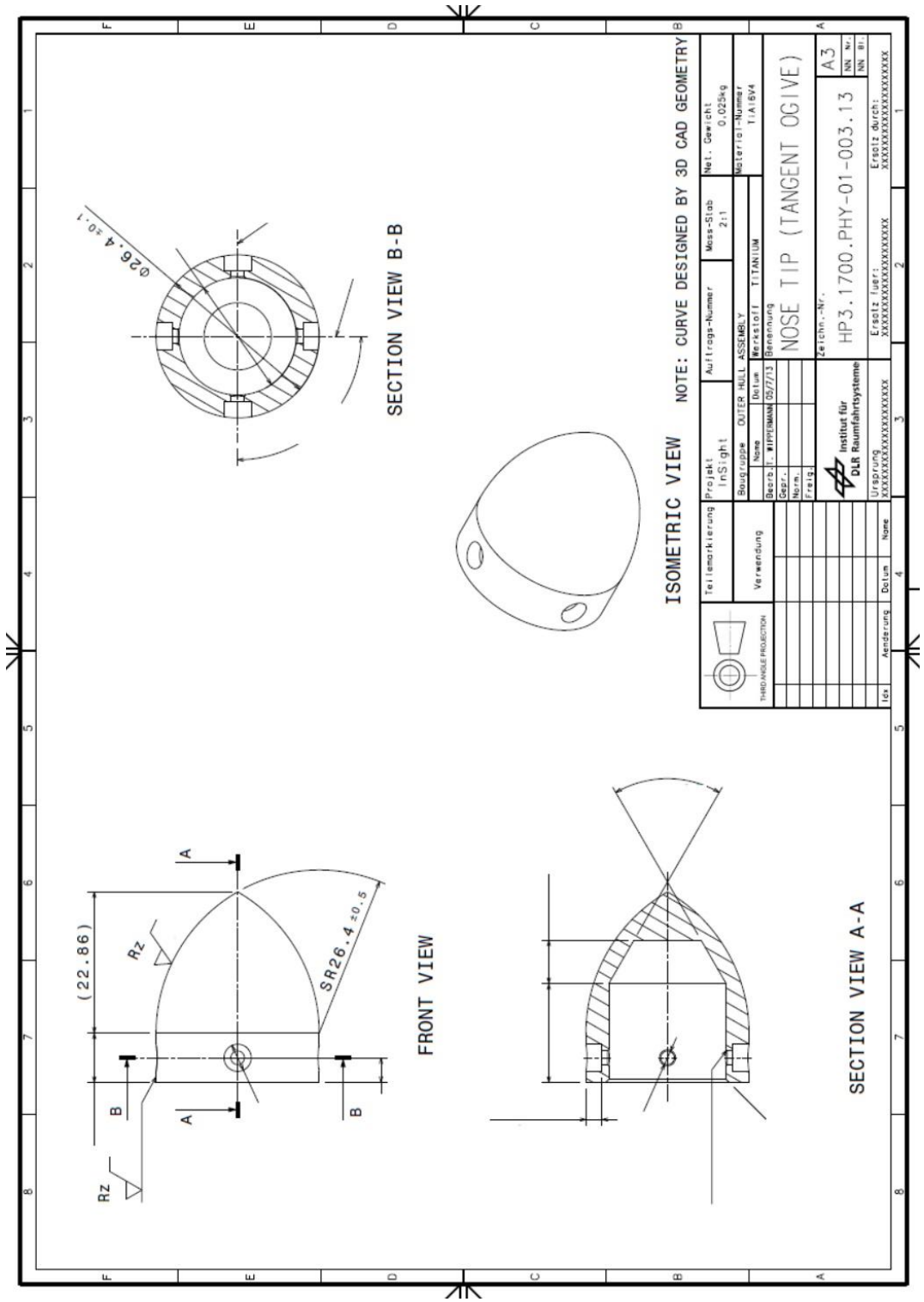

Drawing of the secant tip with removed measurements:

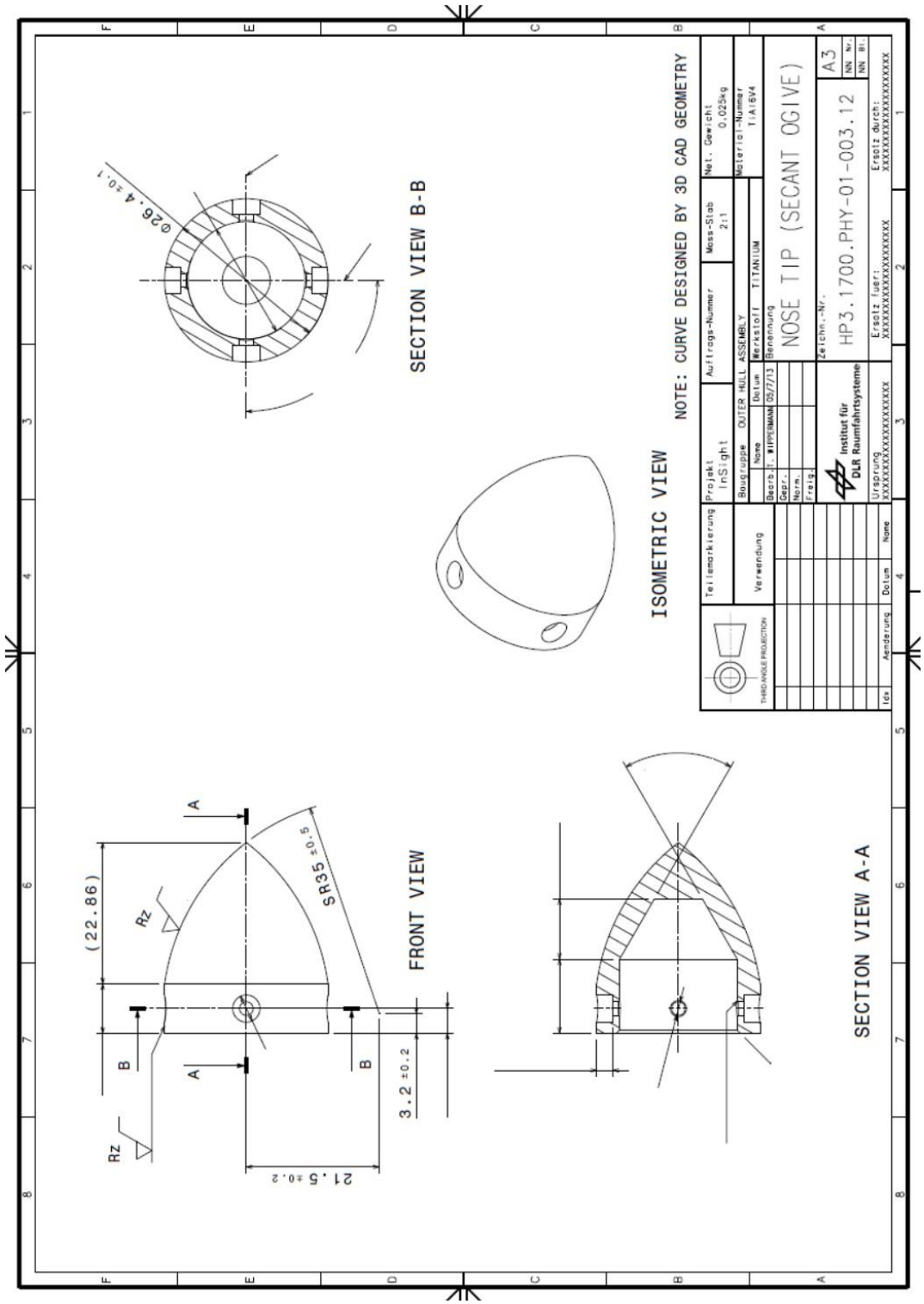

Drawing of the HAACK tip with removed measurements:

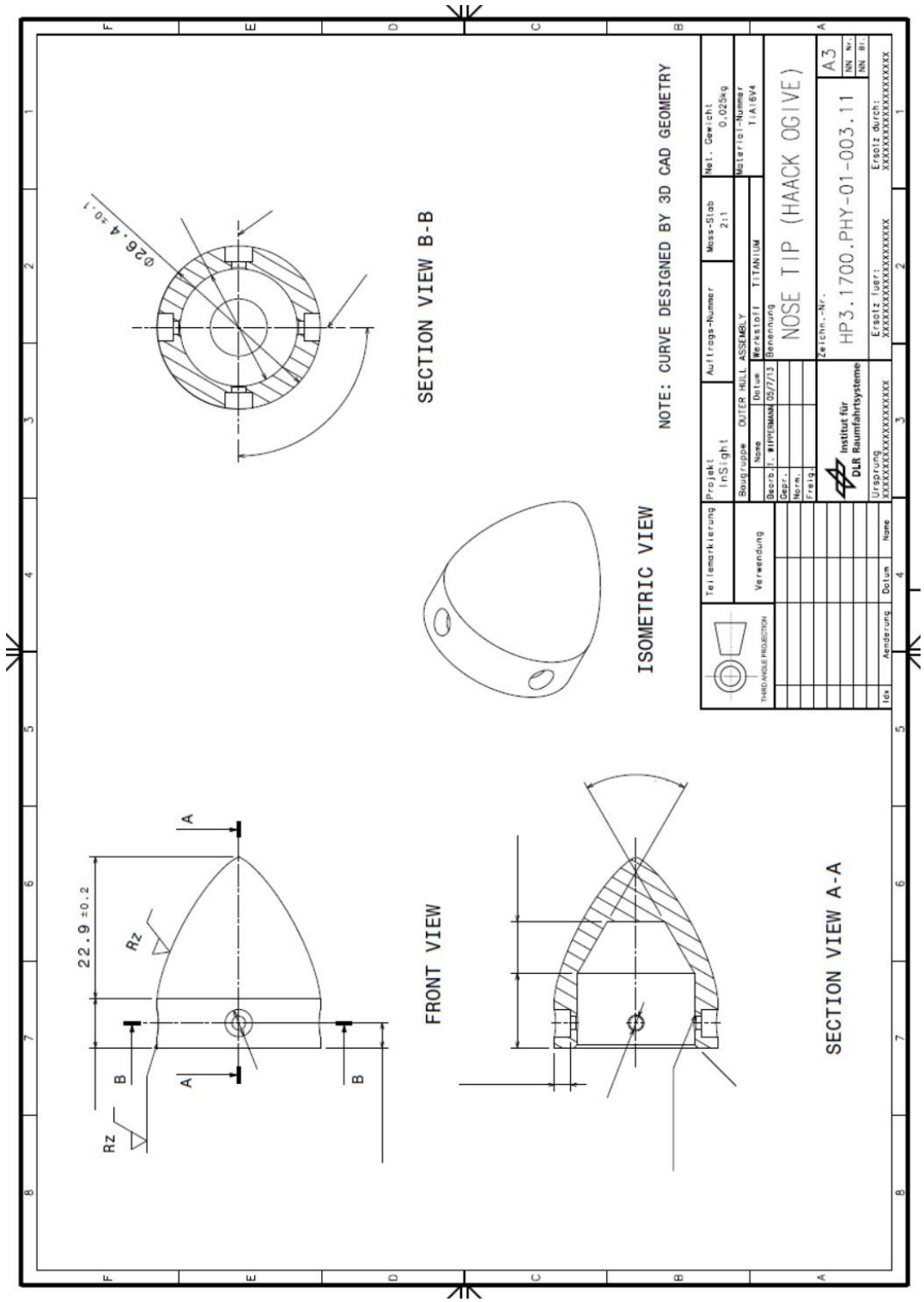

Drawing of the equal pressure tip with removed measurements:

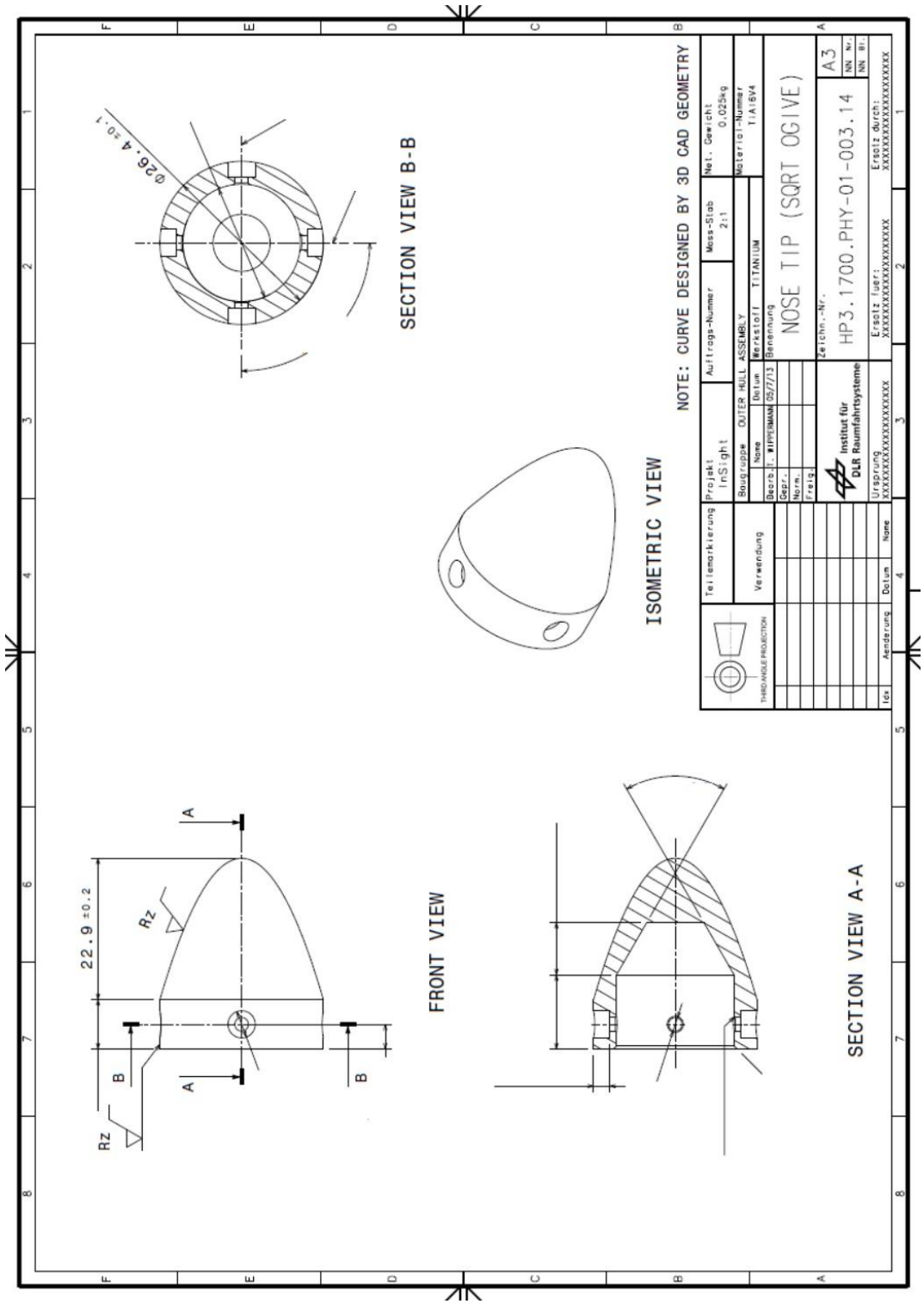

Drawing of the conical tip with removed measurements:

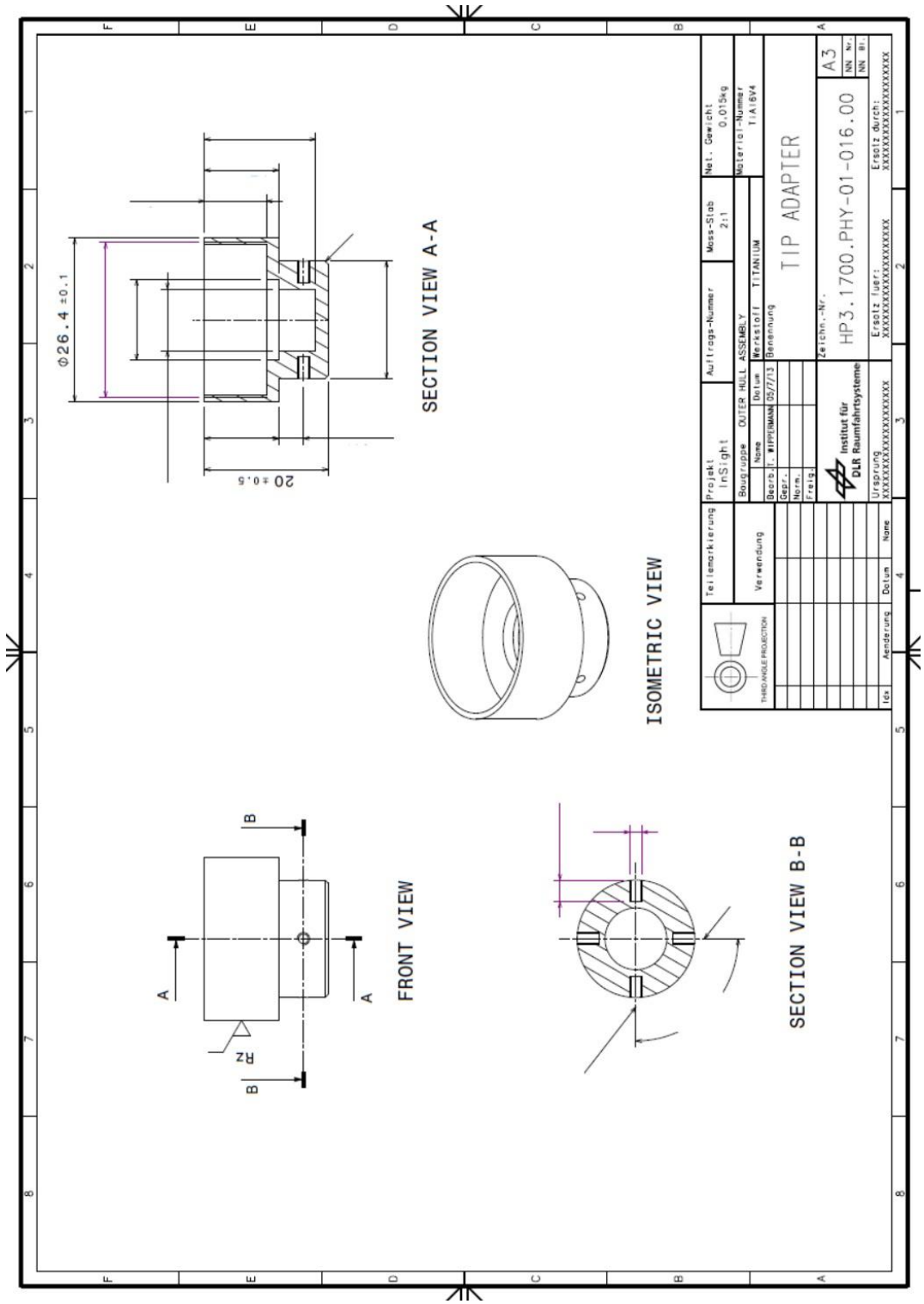

Appendix E Deutsche Zusammenfassung

1. Einführung

Das Thema dieser Diplomarbeit ist die Optimierung des HP³-Moles. Dies ist ein rotationsloser Bohrer, der von dem Deutschen Zentrum für Luft- und Raumfahrt entwickelt wurde und für die InSight-Mission eingesetzt werden soll. Im Rahmen dieser Mission wird das HP³-System (Heat Flow and Physical Properties Package) zum Mars geflogen und auf dessen Oberfläche abgesetzt. Hierfür wird ein Lander, der auf dem Phönix-Lander basiert, benutzt. Auf diesem werden zudem die Instrumente SEIS und RISE verstaut.

Zur Zeit der Durchführung dieser Diplomarbeit wurden mehrere Moles von unterschiedlichen Institutionen entwickelt oder befinden sich in der Entwicklung. Hierbei lassen sich grundsätzlich zwei verschiedene Arten von Moles unterscheiden: Moles zur Probenrückführung an die Oberfläche (z. B. PLUTO) und Moles zur Durchführung von Messungen im Inneren des Himmelskörpers (z. B. MUPUS).

2. Mole-Theorie

Auf dem Marsboden angekommen und nachdem alle System-checks durchgeführt wurden, beginnt der interne Schlagmechanismus des HP³-Moles zu arbeiten. Dies ist ein 3-Massen-System, dass durch zwei Federn zueinander gekoppelt ist. Die Schlagfeder wird durch eine Rolle gespannt, die auf einer zylindrischen Rampe, die Steigungsrampe, hochrollt. Dadurch wird die Hammer Masse, die die Steigungsrampe enthält, zum Aktuator, bei der die Rolle Teil der Baugruppe ist, gezogen. Erreicht die Rolle das Ende der Rampe, kann sich die Schlagfeder wieder entspannen. Dabei beschleunigt sie den Hammer in Richtung des Gehäuses und dieser stößt auf das Gehäuse. Ein Teil der kinetischen Energie des Hamemrs wird dabei auf das Gehäuse übertragen. Dadurch bewegt sich der Mole ein Stück tiefer in den Marsboden. Zeitgleich bewegt sich der Aktuator in die entgegengesetzte Richtung und spannt die Bremsfeder. Diese befindet sich zwischen dem Aktuator und dem Gehäuse. Die Bremsfeder entspannt sich wieder und lässt den Aktuator und den Hammer auf das Gehäuse schlagen. Dadurch wird ein zweites Mal kinetische Energie auf das Gehäuse übertragen und der Mole kommt wieder ein Stück tiefer in den Boden. Danach befinden sich die Massen wieder in der Ausgangslage und ein weiterer Zyklus beginnt mit dem Spannen der Schlagfeder.

Für diesen Prozess lassen sich sechs Parameter zusammenfassen, die diesen beeinflussen: Die Massen des Hammers, des Aktuators und des Gehäuses, die Federkonstanten der Schlag- und der Bremsfeder, sowie die Auslenkung der Schlagfeder.

3. Parameteranalyse

Eine Veränderung bei einer der drei Massen bewirkt eine Verschiebung des optimalen Wertes für die anderen Massen. Um die Massen zu optimieren wird deswegen das Verhältnis der Massen zueinander betrachtet und verbessert. Zunächst wird allerdings für das nächste Model des Moles nur eine begrenzte Veränderung eingebracht, da der Hammer und der Aktuator beibehalten werden. Der optimale Wert für die Gehäusemasse ist 0.145 kg. Dies gibt somit ein Designkriterium für den Prototypen-Mole an, dass die Masse möglichst diesen Wert erreichen soll. Im weiteren wird zunächst das Massenverhältnis nur mit der Einschränkung optimiert, dass das Gesamtgewicht gleichbleiben soll. Ohne diese Vorgabe würden die einzelnen Massen ihr Optimum bei deutlich größeren Werten haben. Das Ergebnis dieser Betrachtung ergibt jedoch unrealistische Werte für den Aktuator aus. Zudem wird das grundlegende Prinzip des Schlagmechanismus verändert, da der erste Stoß durch den Hammer nur noch zum Spannen der Bremsfeder genutzt wird. Um dies zu verhindern, werden andere Einschränkungen gemacht, die teilweise realistische Massen vorgeben. Das Verbesserungspotential durch die erste Veränderung zum Prototyp-Mole beträgt + 38,4 % für die kinetische Energie des Gehäuses im Vergleich zum vorhergehenden Breadboard-Mole. Die weiteren Anpassungen steigern dies noch einmal um 7,9 % (mit unrealistischen Massen), bzw. 3,6 % (mit realistischen Werten).

Die Auslenkung der Schlagfeder müsste auf den größtmöglichen Wert erhöht werden, der durch die gegebenen Bedingungen erreichbar ist, da sie die gespeicherte Energie der Schlagfeder erhöht. Die kinetische Energie des Gehäuses steigt mit steigender Schlagfederenergie. Das Verbesserungspotential liegt hierbei in der Nutzung des maximalen Drehmomentes des Getriebes für einen längeren Zeitraum. Dies kann durch eine Veränderung der Gestalt der Steigungsrampe erreicht werden. Es hat sich hierbei erwiesen, dass eine logarithmische Funktion für die Höhe der Steigungsrampe sehr gut an das maximale Drehmoment herankommt. Dadurch kann die kinetische Energie des Gehäuses um 67,3 % im Vergleich zum PT-Mole verbessert werden.

Durch die Optimierung der Federkonstante der Schlagfeder wird ebenfalls auch die Gestalt der Steigungsrampe verändert. Es kann hierbei eine Steigerung von 79,2 % zum PT-Mole erreicht werden, jedoch auf Kosten einer Erhöhung der Molelänge. Die Bremsfeder hat nach der Mole-Theorie scheinbar keinen großen Einfluss auf die Leistung des Moles. Da dies jedoch nicht mit Beobachtungen aus früheren Tests übereinstimmt, wird die Federkonstante der Bremsfeder nicht verändert.

4. Designveränderungen

In einem ersten Schritt wird der Prototyp-Mole konstruiert. Die Gehäusemasse wird dabei so niedrig wie möglich gehalten während zugleich die Messinstrumente im Inneren des Moles

untergebracht werden. Zudem wird der Außendurchmesser des Moles verkleinert um den Eindringwiderstand des Bodens zu verringern.

Als weitere Veränderung wird die modifizierte Steigungsrampe realisiert. Zudem werden verschiedene Spitzenformen konstruiert, die aufbauend auf anderen Arbeiten den Eindringwiderstand weiter verringern sollen. Da hierzu jedoch keine genauen Daten über das bestmögliche Design bestehen, werden mehrere Spitzen mit unterschiedlichen Formen entwickelt. Diese sollen später getestet werden, wobei dafür ein möglichst einfaches Austauschen der Spitzen möglich sein sollte. Deshalb wird außerdem ein Adapter für die Spitzen konstruiert. Die verbesserte Steigungsrampe und die Spitzen werden bei einem PT-Mole angewandt werden. Da dies jedoch nicht zum eigentlichen Konzept gehört, wird dieser Mole Hybrid genannt.

5. Belastungsberechnung

Durch die erhöhten Energien der Federn und der Stöße sind auch die Materialbelastungen größer. Um sicher zu gehen, dass die Bauteile trotzdem ausreichend ausgelegt sind, werden die Belastungen bei kritischen Bauteilen nachgerechnet. Es wird gezeigt, dass diese Bauteile eine ausreichende Sicherheit gegen Versagen haben.

6. Validierung der Verbesserungen

Um die errechneten Verbesserungen zu bestätigen wird ein Teststand konstruiert, der relativ einfach und schnell eine Aussage über die Leistungsfähigkeit machen kann. Hierfür wird der Mole auf eine Halterung auf einer Feder gesetzt und die Auslenkung durch die Schläge mittels eines Abstandssensors gemessen. Der Teststand führt dabei auch den Mole damit dieser zentriert auf der Feder positioniert ist. Um die erhaltenen Ergebnisse auch in die kinetische Energie des Gehäuses umgerechnet werden kann, müssen die Reibungsverluste in dem Teststand bestimmt werden. Erste Tests mit dem BB-Mole und dem PT-Mole zeigen, dass diese wahrscheinlich einen großen Einfluss auf die Messwerte haben. Zudem ist dennoch die Energie der Teststandfeder deutlich geringer als es die Theorie vermuten lässt. Daraus ergibt sich, dass die Theorie noch weitere Verbesserungen benötigt.

Die Tests mit dem Hybrid-Mole müssen noch durchgeführt werden. Hierbei kann lediglich der Einfluss der Steigungsrampe in dem Teststand analysiert werden. Die Verbesserung durch die verschiedenen Spitzen ist nur in einem Penetrationstest möglich. Ebenso verhält es ich mit dem einfluss des kleineren Außendurchemssers des Moles bei dem PT-Mole.

Trotz alle dem konnte eine deutliche Verbesserung von dem BB-Mole zum PT-Mole mit Hilfe des Teststandes bestätigt werden.

Appendix F Project files

The project files contain the Work Breakdown Structure, the timeline and the Work Package Description.

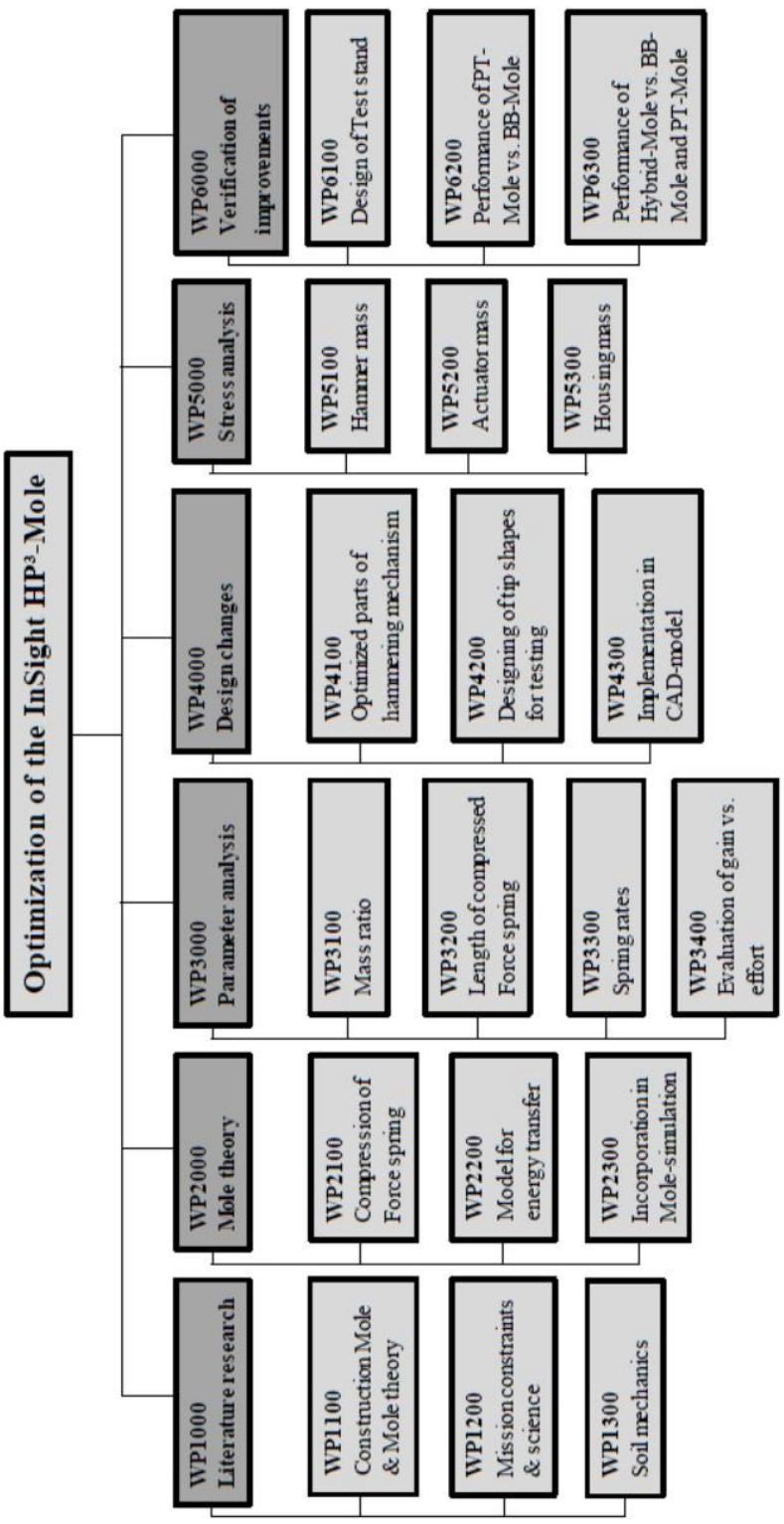

n

(Zeitplan, eine Seite)

o

(“Work package description”, 19 Seiten)